Ceramics International 52 (2026) 18169–18186

Contents lists available at ScienceDirect

Ceramics International

journal homepage: www.elsevier.com/locate/ceramint

Understanding microstructure evolution of cast geopolymers based on metakaolin and ceramic tile waste

Giulia Masi *, Carlotta Pacente, Lucia Ferrari, Anastasiia Nagmutdinova, Elisa Franzoni, Maria Chiara Bignozzi

Department of Civil, Chemical, Environmental and Materials Engineering, University of Bologna, Via Terracini 28, 40131, Bologna, Italy

ARTICLE INFO

Keywords:
Ceramic waste
Alkali activated materials
Porosity
Mercury intrusion porosimetry
^{1}H low field
Nuclear magnetic resonance (TD NMR)

ABSTRACT

This study addresses the current lack of insight into the microstructure evolution of cast geopolymers produced by combining two different precursors. Detailed investigations of micro- and nano-porosity developed during geopolymerization as a function of curing time are carried out and, for the first time, ^{1}H Time-Domain Nuclear Magnetic Resonance is applied diffusely. The results show that the metakaolin replacement with 35% ceramic tile waste addition induces coarsening of pore size distributions in the 0.08-1 μm range and a reduction in gel content. Furthermore, although a delay in the development of the 3D network was observed, the gel formation process was still completed within 24 h, in contrast to the 5–6 h required for 100% metakaolin geopolymers. These differences in microstructural evolution are also reflected in the development of compressive strength.

1. Introduction

Geopolymers and alkali activated materials (AAM) are aluminosilicate systems that have achieved large scientific interest in the last 20 years, thanks to their excellent mechanical, high-temperature and durability performances [1–4]. One key aspect of geopolymer and AAMs is the possibility to use industrial waste as components in addition to metakaolin (MTK), which is the major precursor applied [5]. Thus, several industrial wastes, e.g. fly ash [6–9], ground granulated blast-furnace slag (GGBS) [10–13] and red mud [14–17], were largely applied as precursors or activators in alkali activated technology, to enlarge the environmental sustainability and to apply circular economy concepts [18]. In addition, previous studies have investigated the combination of different precursors, e.g. metakaolin and fly ash [19–21]. This combination led to a decrease in the average precursor reactivity and thus a slowing down of the geopolymerization [19,20]. However, a combination of metakaolin and fly ash microspheres induced a positive effect in terms of microstructure densification, in view of the formation of C-A-S-H phases [21].

One emerging source suitable as a precursor for alkali activation is ceramic waste [22] from tiles, bricks, sanitary ware, pottery, or refractory production [23–27]. Ceramic waste can be sourced as construction and demolition waste (CDW) [28,29] or from ceramic industry processes [30]. The suitability of different ceramic waste for alkali activation was already demonstrated by Deng et al. [31]. Moreover, different types of ceramic tile waste have already been used as a precursor for alkali activation. In a previous study [20], rectifying porcelain stoneware tile powder was used as a precursor to develop lightweight composites with thermal conductivities comparable to commercial cementitious foams. Similarly, Horvat and Ducman [32] used green tile body residue to prepare alkali activated foams with compressive strengths greater than 1 MPa by investigating several direct foaming techniques. Mechanical characterization of alkali activated mortars with ceramic tile waste and recycled glass powders was performed by Bilondi et al. [33], which showed a compressive strength of about 25 MPa after 28 days of curing for the optimized mix. Ceramic waste has been applied as a precursor or aggregate in alkali activation for several applications, such as high temperature applications [24–26,34], mortar and concrete [35–38], repair and restoration [27,39] and radiological mitigation [40]. Although many publications are available, a knowledge gap remains regarding how geopolymer microstructure evolves at early and late (28 days) curing times when 100% metakaolin or a blend of metakaolin and ceramic waste is used as a precursor.

For investigating microstructural evolution, open porosity measurements are usually reported by means of mercury intrusion porosimetry (MIP) measurements; however, only pore size distributions in the range 0.01 – 100 μm are considered [9,41–43]. Fewer investigations are carried out on porosity at the nano-metric level, mainly using nitrogen

* Corresponding author.
E-mail address: giulia.masi5@unibo.it (G. Masi).

https://doi.org/10.1016/j.ceramint.2026.02.377
Received 24 December 2025; Received in revised form 17 February 2026; Accepted 24 February 2026
Available online 24 February 2026

Table 1
Chemical composition (wt%) of the selected precursors (LOI and bdl stand for loss of ignition and below detection limit, respectively).

	SiO_2	Al_2O_3	TiO_2	Fe_2O_3	CaO	MgO	K_2O	Na_2O	Cr_2O_3	ZrO_2	SO_3	LOI
CTW	73.2	17.5	0.8	1.1	1.5	0.5	1.9	2.9	*bdl*	0.4	0.1	0.4
MTK	72.0	22.1	1.0	1.6	0.4	0.1	0.3	0.04	0.02	*bdl*	*bdl*	2.4

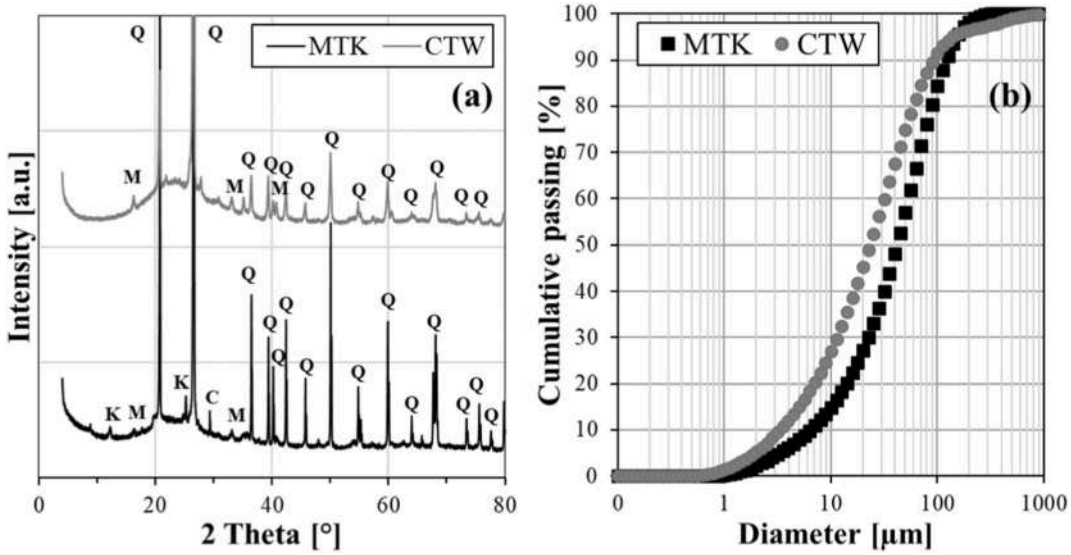

Fig. 1. (a) XRD patterns (C = calcite; K = kaolinite; M = mullite; Q = quartz) and (b) particle size distributions of MTK and CTW.

Table 2
Particle size distribution in µm of the selected precursors.

	d(10) (µm)	d(50) (µm)	d(90) (µm)
CTW	3.3	23.3	91.4
MTK	6.5	41.9	121.1

(N_2) adsorption/desorption isotherms. It has been found that MTK geopolymers usually exhibit a type IV isotherm with a hysteresis loop [44–48], according to the classification reported in Refs. [49,50]. Duxson et al. [44] also highlighted that increasing the Si/Al ratio (from 1.15 to 2.15) in MTK-based geopolymers leads to a smaller volume of adsorbed N_2, thus indicating a denser 3D network. Other studies [45,46] mainly found a mesoporous microstructure formed by the aggregation of lamellar particles. A less conventional method to characterise porosity is ^{1}H Time-Domain Nuclear Magnetic Resonance (^{1}H TD-NMR). This powerful analytical tool enables non-invasive and non-destructive detection of the pore size distribution, essential for detecting gel nano-porosity and understanding microstructural evolution [51,52]. By this technique, important insights into cement hydration reactions, also including limestone calcined clay cements (LC3), have already been published [51,53,54], by offering real-time monitoring of the evolution of water-filled pores and phase development. So far, ^{1}H TD-NMR has been scarcely used for the characterization of geopolymers, with applications limited to alkali-activated slag binders [55] and MTK-based geopolymer [56,57]. In the latter, studies focused on understanding the effects of various silicate moduli at an early age [57] and on how the Si/Al ratio affects the geopolymerization reaction as observed by a single-sided NMR device. However, the effect of combining two precursors, one of which is MTK, has never been analysed by ^{1}H TD-NMR. Indeed, despite recent advances in characterizing geopolymer systems, significant gaps remain in understanding how the combination of chemically distinct precursors affects curing mechanisms and pore structure evolution. In particular, although differences in water distribution and pore connectivity have been observed in various systems [58,59], the specific impact of dual-precursor formulations on multiscale porosity has not been systematically addressed yet. Moreover, reviews on metakaolin-based porous geopolymers highlight the complexity of pore architecture and the necessity of employing complementary techniques to capture its full extent [60]. Each of the presented methods probes distinct pore domains and relies on different physical assumptions: MIP is sensitive to pore entry sizes and connectivity, N_2 adsorption provides access to mesopores and specific surface area under dried conditions, while ^{1}H TD-NMR captures the distribution of water-filled pores in a non-destructive manner. Therefore, their combined application is essential to achieve a comprehensive understanding of pore structure evolution in dual-precursor geopolymer systems.

For all these reasons, this paper reports a systematic study of different characterization techniques for investigating the porosity evolution by means of the curing time. Thus, the aim is to fulfil the above-mentioned gap in understanding the influence of combining precursors, especially related to the partial replacement of MTK with ceramic tile waste powder (CTW). To do this, a constant MTK replacement amount was considered and compared to the 100% MTK-based geopolymers. For each formulation, three different water/solid ratios (w/s: 0.36, 0.39 and 0.42) were adopted to produce geopolymer mixes suitable for casting forming methods. All the geopolymers were investigated by a multi-analytical approach based on three different techniques, such as MIP, N_2 adsorption test and ^{1}H TD-NMR applied at various curing times (2, 7 and 28 days). In the case of ^{1}H TD-NMR, further measurements were carried out starting 0.5 h after mixing procedures. These results provide interesting insights into the pore structure and the 3D network formation at the onset of geopolymer formation. The combined use of MIP, N_2 adsorption, and ^{1}H TD-NMR in this study goes beyond a parallel application of established techniques and it is specifically designed to understand the multiscale porosity of MTK-based and dual-precursor geopolymers. By integrating and critically comparing the outputs of these techniques, this work provides a

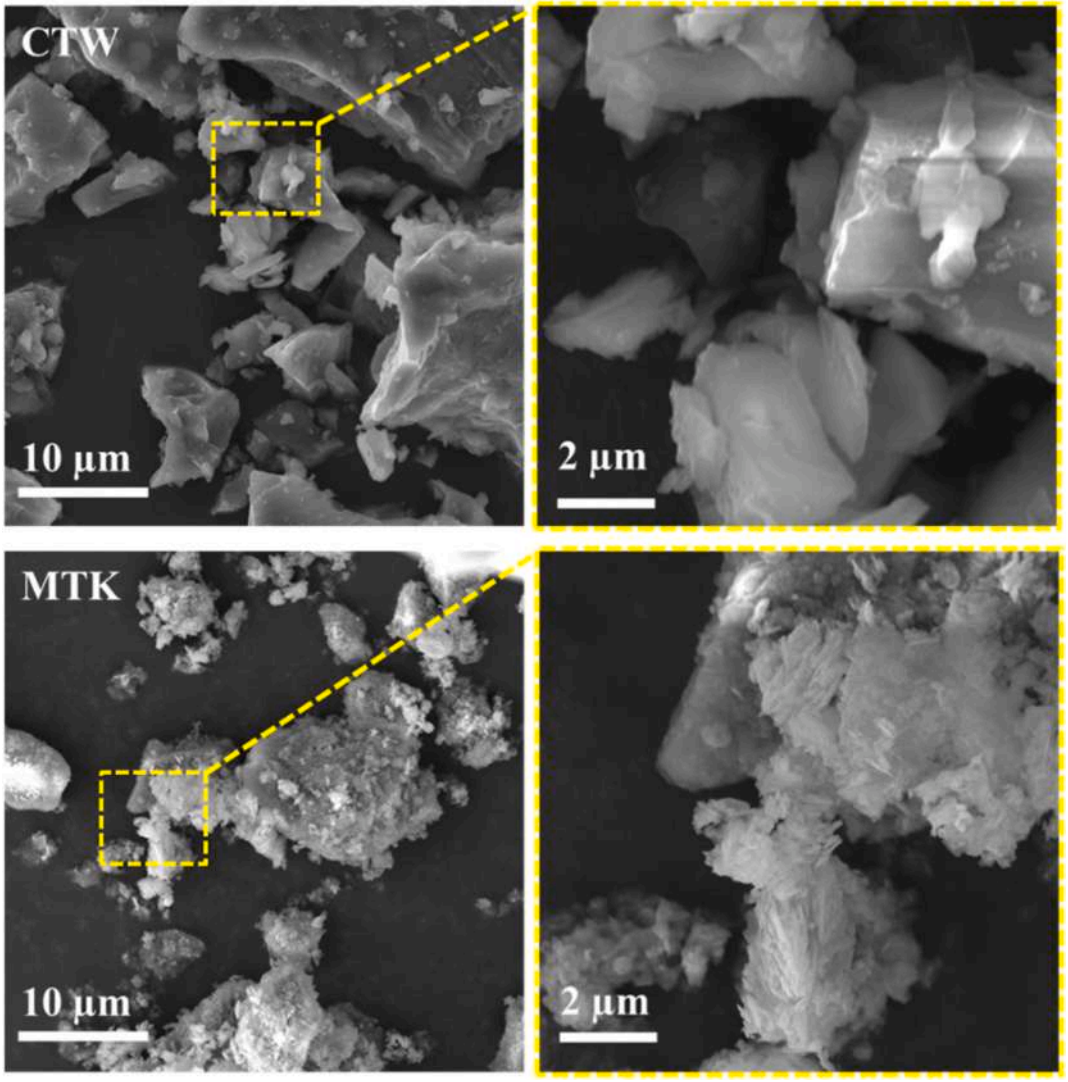

Fig. 2. SEM observation of precursors (CTW and MTK) using secondary electrons.

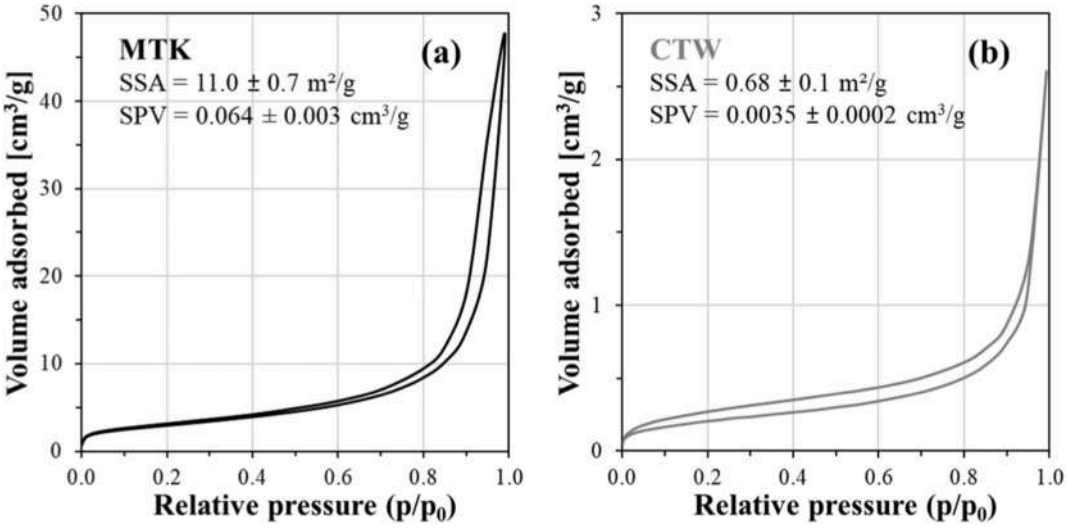

Fig. 3. N_2 adsorption and desorption isotherms of the dry (a) MTK and (b) CTW. Values of SSA and SPV are reported in the plots.

Table 3
Formulations (wt%) of the prepared samples. Theoretical molar ratios and w/s ratios are also reported (only amorphous silica is considered).

	MTK	CTW	8M NaOH	Na_2SiO_3 solution	SiO_2/Al_2O_3	Na_2O/Al_2O_3	Na_2O/SiO_2	w/s
R42	37.4	21.0	11.9	29.7	2.3	0.7	0.3	0.42
MK42	58.4	-	11.9	29.7	1.8	0.6	0.4	
R39	38.7	21.7	11.3	28.2	2.3	0.6	0.3	0.39
MK39	60.5	-	11.3	28.2	1.8	0.6	0.3	
R36	39.8	22.3	10.8	27.1	2.2	0.6	0.3	0.36
MK36	62.1	-	10.8	27.1	1.8	0.6	0.3	

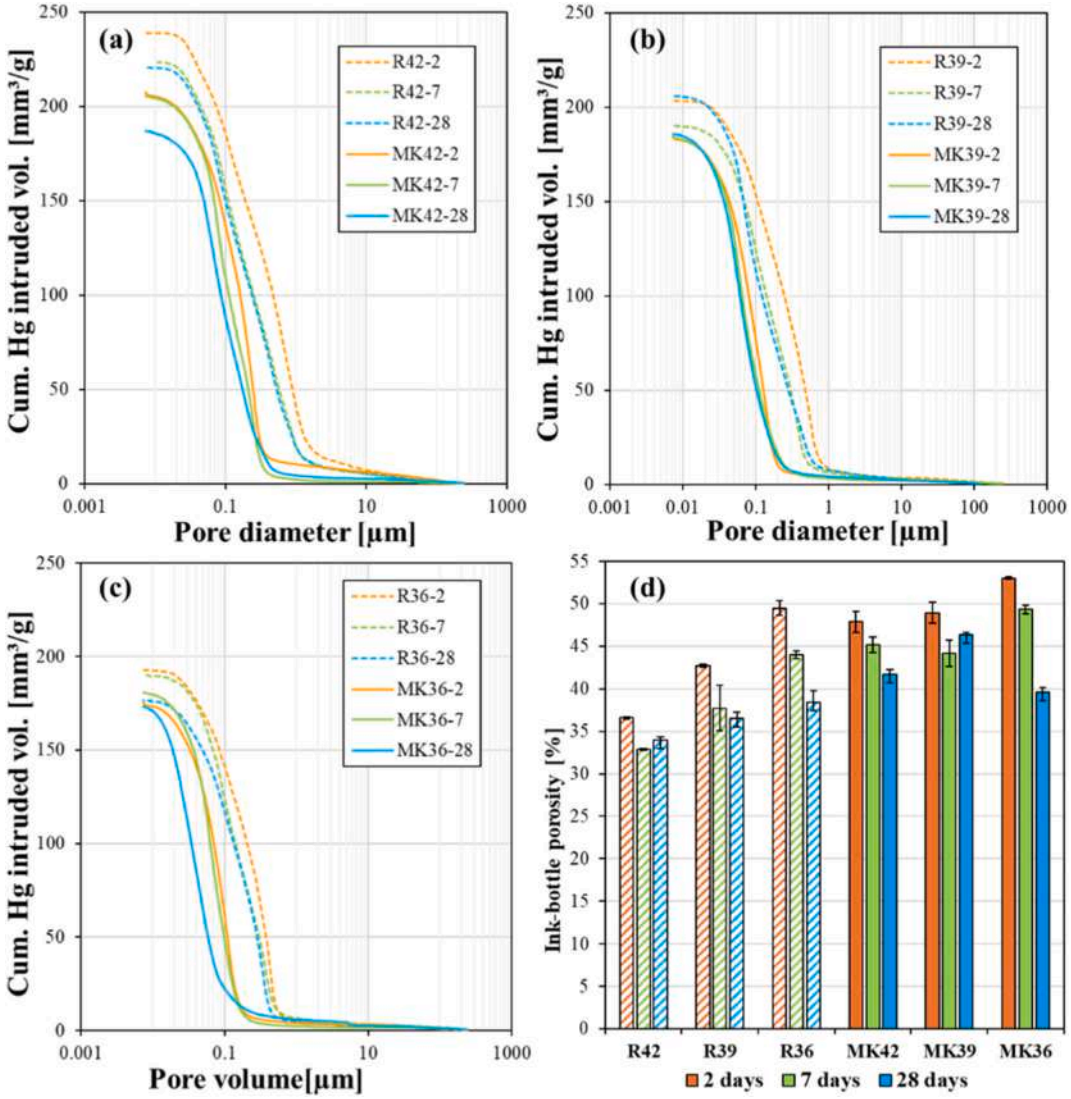

Fig. 4. Cumulative pore size distribution by MIP of the samples after a curing period of 2 days in orange, 7 days in green, 28 days in light-blue: (a) R42 (dotted lines) and MK42 (solid lines); (b) R39 (dotted lines) and MK39 (solid lines); (c) R36 (dotted lines) and MK36 (solid lines); (d) "ink-bottle" porosity. (For interpretation of the references to colour in this figure legend, the reader is referred to the Web version of this article.)

comprehensive and previously unavailable interpretation of pore size distribution and pore morphology, enabling new insights into how precursor blending governs pore structure evolution. Results of Fourier Transform Infrared Spectroscopy (FT-IR), X-ray diffraction (XRD) and Field Emission Gun-Scanning Electron Microscopy (FEG-SEM) coupled with Energy Dispersive X-ray Spectroscopy (EDS) are also reported to discuss the microstructural evolution with respect to curing times. Finally, the performance of the obtained formulations in terms of compressive strength is considered to highlight correlations between macroscale properties and microstructure investigations.

2. Materials and methods

2.1. Materials

The following precursors were used for the preparation of geopolymers: metakaolin (MTK) sourced from ARGECO Développement (France) and ceramic tile waste powder (CTW), kindly supplied by Ascot Evertile (Italy). MTK is produced by flash calcination, a firing process where kaolinite particles are transformed into metakaolin by passing near a flame for a few tenths of a second at approximately 700 °C [61]. CTW is a waste sourced from the rectifying process of fired porcelain

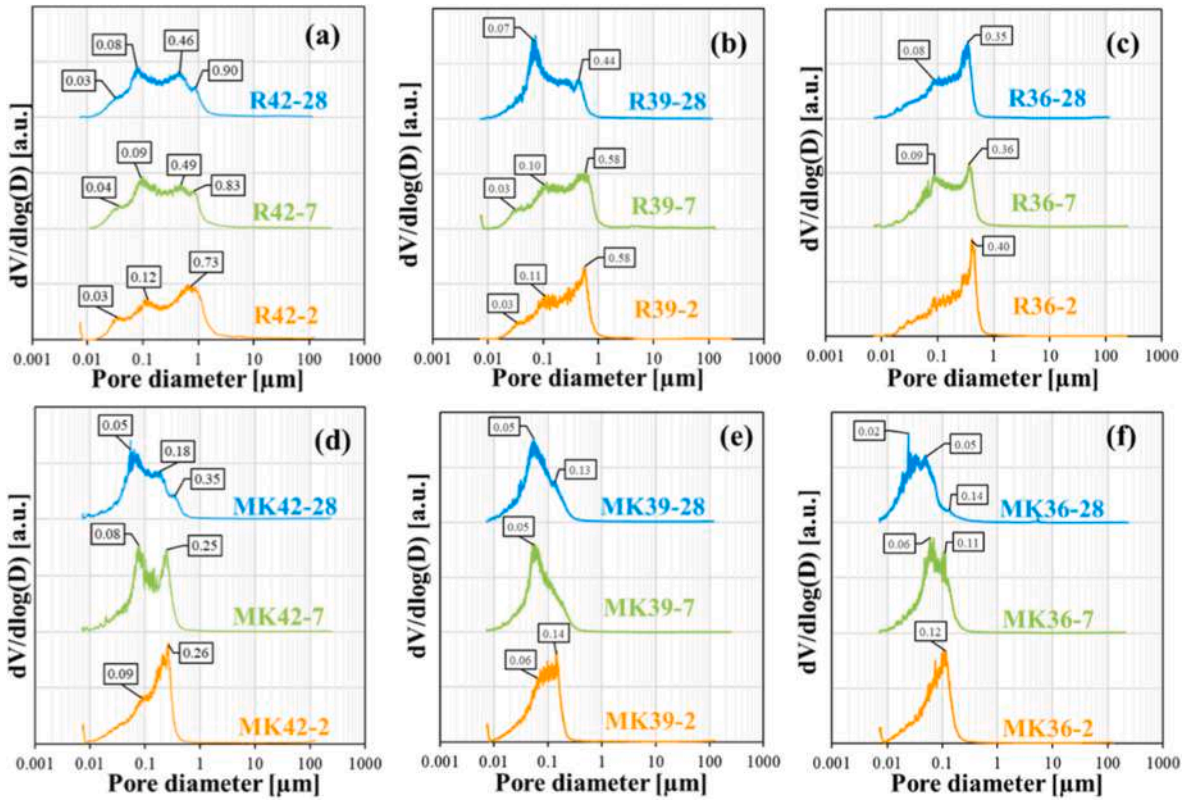

Fig. 5. Pore size distribution by MIP of the geopolymer samples after a curing time of 2 days in orange, 7 days in green and 28 days in light-blue: (a) R42, (b) R39, (c) R36, (d) MK42, (e) MK39 and (f) MK36. The main characteristic populations of pore size are labelled for each plot. (For interpretation of the references to colour in this figure legend, the reader is referred to the Web version of this article.)

stoneware tiles and its amount can be estimated at around 30.000 tons/year in Italy [27]. Table 1 reports the chemical composition of both precursors, measured by using ICP-OES (PerkinElmer, Avio 550 MAX).

From the mineralogical point of view, MTK is composed predominantly of quartz, with calcite, kaolinite and mullite present in traces. The amorphous silica content is 29%, as reported in a previous study [62]. CTW is composed mainly of quartz and mullite, with an amorphous silica fraction of approximately 50%, as determined by quantitative X-ray diffraction (XRD) [20]. XRD patterns of MTK and CTW are reported in Fig. 1a. The particle size distribution of the precursors was obtained by using a laser diffraction particle size analyser (Mastersizer 2000, Malvern Instruments). Particle size distributions of MTK and CTW are reported in Fig. 1b, with the characteristic values in Table 2.

The morphology of both precursors observed with a Field Emission Scanning Electron Microscope (FEG-SEM, Tescan, Mira 3) is displayed in Fig. 2. CTW exhibits angular shapes and sharp edges due to the rectifying processes of porcelain stoneware tiles after firing. The MTK shows agglomerated particles due to the flash calcination process [63,64] and displays its typical lamellar morphology at high magnification. FEG SEM observations show that the larger dimensions of MTK determined by laser granulometry are mainly caused by agglomeration. Finally, the specific surface area (SSA) and specific pore volume (SPV) were determined by Anton Paar NOVA 800, a N_2 adsorption with a Brunauer–Emmett–Teller, BET, surface area analyser [65]. MTK and CTW samples (~0.5 g) were first degassed for 1 h at 100 °C to remove residual moisture and then analysed with N_2 adsorption/desorption. SSA and SPV data, as well as N_2 isotherms, are reported in Fig. 3. MTK exhibits significantly higher values of SSA and SPV compared to CTW, suggesting a difference in the reactivity of the two precursors during geopolymerization.

Alkaline solutions were prepared by dissolving sodium hydroxide (NaOH, supplied by Sigma-Aldrich, ACS reagent) in deionized water to obtain an 8M NaOH solution. A sodium silicate solution (Na_2SiO_3, ReofluxB), supplied by Ingessil S.r.l. (Italy), was used, with a composition of 29.9% SiO_2, 14.4% Na_2O, and 55.7% H_2O.

2.2. Sample preparation

Different formulations were obtained by combining MTK and CWT as reported in Table 3. Samples named MK and R were prepared, respectively, with 100% metakaolin and with 65% MTK +35% CTW, as precursors. The w/s ratio was varied as follows: 0.36, 0.39 and 0.42. The theoretical molar ratios of amorphous SiO_2/Al_2O_3, Na_2O/Al_2O_3 and Na_2O/amorphous SiO_2 slightly differ when ceramic tile waste is used as a precursor compared to when 100% MTK is used (Table 3). The following nomenclature has been applied: the acronyms, MK and R, are followed by the w/s ratio value multiplied by 100. For example, R36 stands for the mix composed of MTK and CTW with a w/s ratio equal to 0.36.

Samples were prepared by mixing one or both of the precursors with activating solutions. After 3 min at low speed, the mixer was stopped for 30 s to detach the material from the mixer walls. A further mixing of 3 min at high speed completed the procedure. A laboratory stirrer (IKA RW20, Germany) was used for mixing volumes up to 0.5 L, while a Hobart mixer (mortar mixer, Matest, Italy) was used to mix 2.0 L. The mixes were cast into plastic cylindrical moulds (diameter = 35 mm, height = 20 mm) or beam moulds (40 mm × 40 mm × 160 mm) and cured for 2, 7 and 28 days at room temperature under sealed conditions, with samples hermetically closed in plastic bags.

2.3. Methods

Mercury Intrusion porosimetry (MIP): Open porosity measurements were carried out by using a mercury intrusion porosimeter (MIP) and N_2

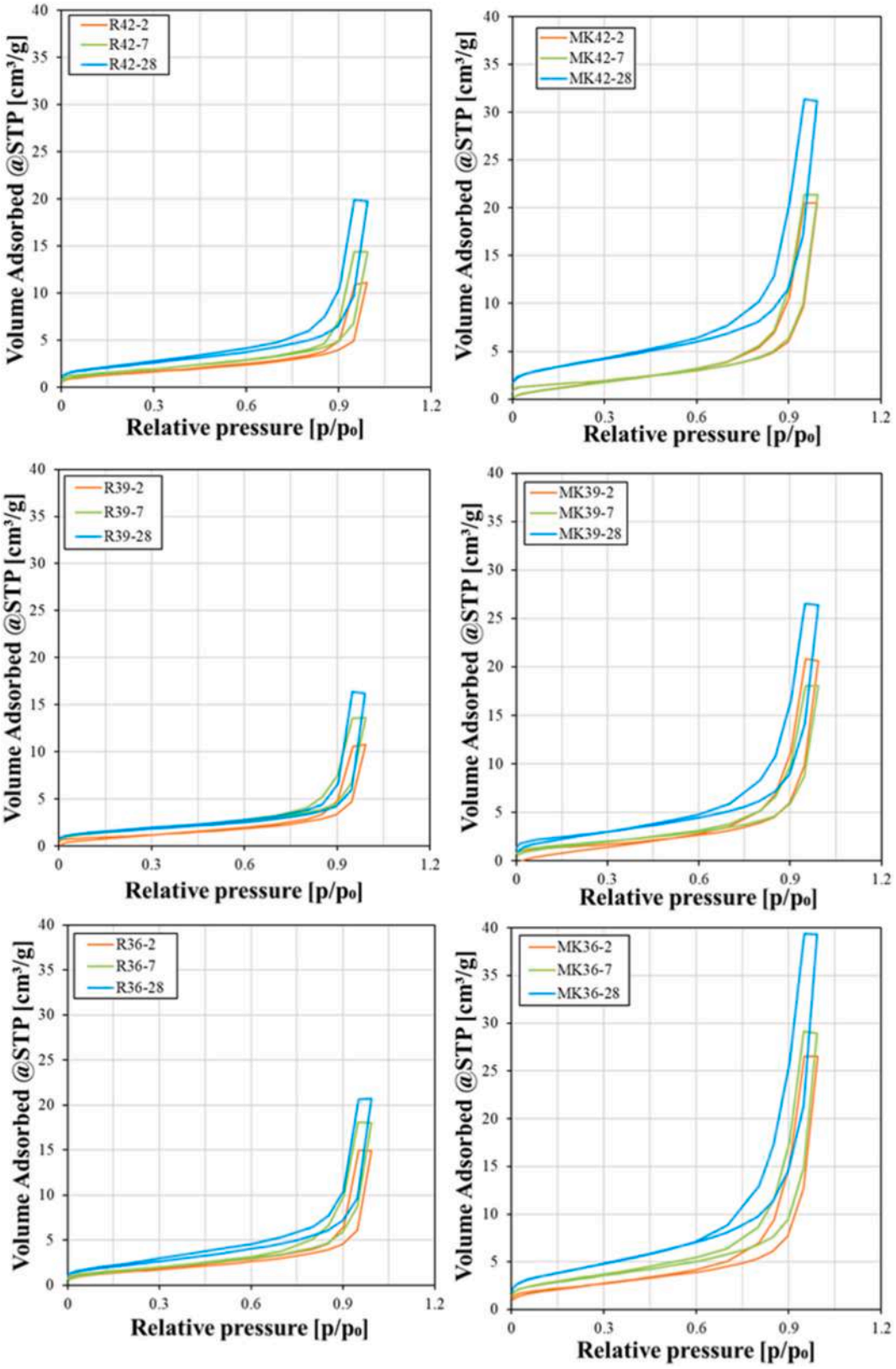

Fig. 6. N_2 adsorption–desorption isotherms of the tested geopolymers at different curing times (2, 7 and 28 days).

adsorption. Before testing, samples were dried in a ventilated oven at 80 °C until constant mass was reached.

MIP measurements were carried out on samples of about 1 cm^3 prepared by avoiding the external surfaces. At least three measurements were taken to verify repeatability. Thermo Scientific Pascal 140 and 240 Mercury Porosimeters instruments were used by applying a pressure between 0.1 kPa and 200 MPa. A Hg contact angle equal to 141.3° and a Hg surface tension (γ) of 0.48 N/m were considered. The detection limit

Table 4
Total cumulative pore volume for R- and MK-geopolymers derived by N_2 adsorption test.

	Cumulative pore volume (cm^3/g)		
	R42	R39	R36
@ 2 days of curing	0.015	0.015	0.020
@ 7 days of curing	0.019	0.019	0.025
@ 28 days of curing	0.027	0.022	0.029
	MK42	**MK39**	**MK36**
@ 2 days of curing	0.027	0.028	0.036
@ 7 days of curing	0.029	0.030	0.040
@ 28 days of curing	0.048	0.036	0.055

of the measurement reached pore sizes in the range of 7 nm – 120 μm. The data elaboration was carried out by S.O.L.I.D. software (SOLver of Intrusion Data, Thermo Scientific). It is important to note that, although the MIP technique is frequently applied to cementitious and alkali activated materials [7,66–68], the pore size distribution determined by MIP comprises both "effective" porosity and "ink-bottle" porosity [68]. The authors are aware of this technical limitation, which was considered in the results' discussion.

N_2 sorption test: The N_2 sorption test was carried out on the geopolymers by preparing small fragments (about 0.5 g) of the internal portion of the samples, thus excluding their outer surfaces. For each geopolymer, at least four samples were tested to verify the measurement reproducibility. The samples were first dried at 100 °C in an oven for at least 24 h. Later, dry samples were first degassed under vacuum for 1 h at 100 °C. Complete N_2 isotherm (adsorption and desorption branch) curves were measured by using an Anton Paar NOVA 800. Pore size distribution was calculated by applying the Density functional theory (DFT) model by Kaomi for Nova PC software [69]. Detectable pore size diameter varies from 2 to 80 nm.

^{1}H Time-Domain Nuclear Magnetic Resonance (^{1}H TD-NMR): The evolution of the water distribution inside the porous structure was analysed by ^{1}H TD-NMR, starting from a curing time of 30 min until 28 days. Measurements were performed with a relaxometry composed of a permanent magnet (Artoscan, Esaote SpA, Italy) with a magnetic field $B_0 \approx 0.2$ T (corresponding to ^{1}H Larmor frequency ≈ 8 MHz), a 10 mm solenoid coil, and a console (Stelar, Italy) at 25 °C. The 90° pulse width of the spectrometer was 4.5 μs, dead time was 25 μs. The T_2 relaxation time was measured using the Carr-Purcell-Meiboom-Gill sequence, with the number of echoes ranging from 256 to 1024, depending on the saturation level of the samples, with an echo time of 60 μs and 200 – 400 scans, depending on the curing time. The low limit of pore size detection is nearly 0.1 ms, corresponding to pores of 1 nm. The quasi-continuous T_2 distribution was calculated using the UpenWin software, developed by a research group at the University of Bologna, based on inversion of multiexponential decay data [70]. The analysis was carried out on all the formulations reported in Table 3. Batches of approximately 200 g were prepared and about 1 g was placed inside a glass tube and sealed for analysis. Each mix was measured at 0.5, 1, 1.5, 2, 2.5, 3, 5, 6, 24, and 48 h, as well as at 7 and 28 days.

Fourier Transform Infrared Spectroscopy (FT-IR): Assessment of the geopolymeric 3D network formation and microstructural evolution was performed by applying Fourier Transform Infrared Spectroscopy (FT-IR) and Field Emission Gun – Scanning Electron Microscopy (FEG-SEM) techniques. FT-IR was carried out using a PerkinElmer Spectrum Two instrument, in ATR mode, in the range of 2000 – 400 cm^{-1}, with a spectral resolution of 4 cm^{-1}. The FT-IR spectra were obtained by acquiring 16 scans and a data interval of 1 cm^{-1}.

X-ray diffraction (XRD): The mineralogical composition of geopolymer samples was determined by X-ray diffractometry (XRD), using a PANalytical X'Pert PRO powder diffractometer equipped with a fast X'Celerator detector. The experimental parameters are as follows: Cu-Kα radiation, 40 kV and 30 mA, 2θ range from 4° to 80° with a time/step of

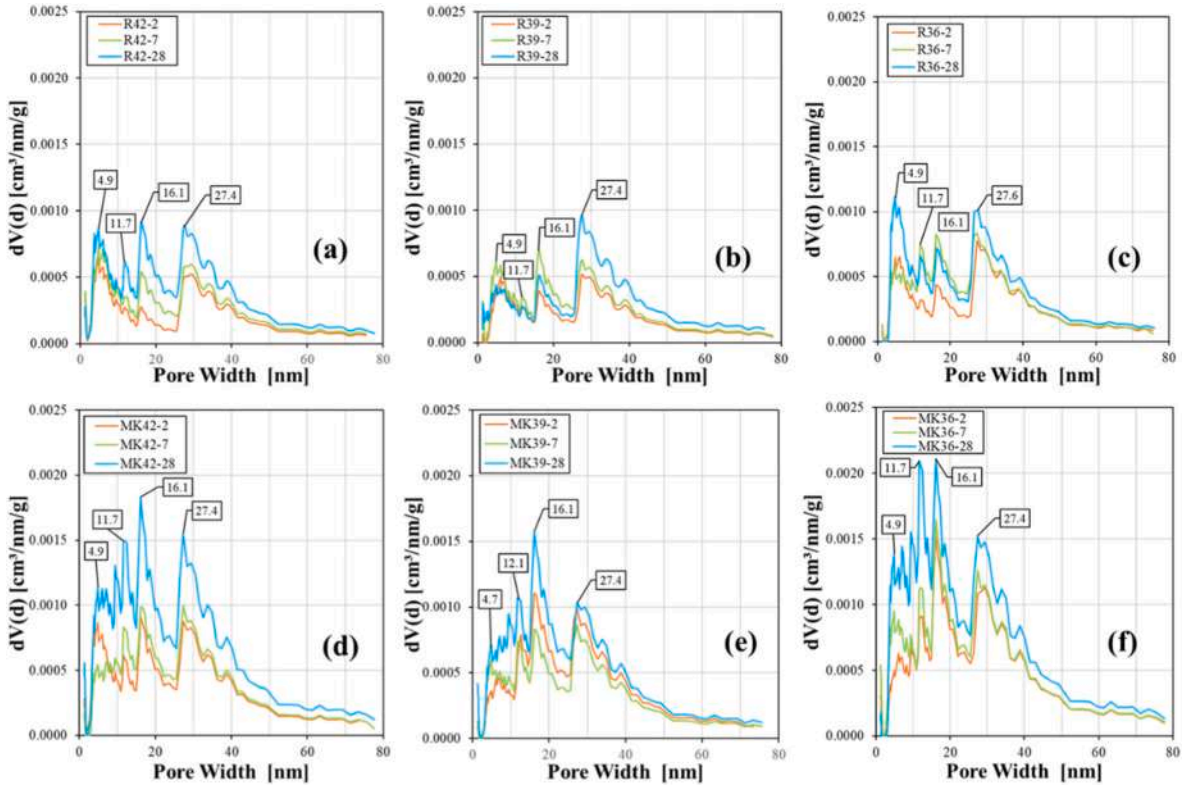

Fig. 7. Derivative pore size distribution by N_2 adsorption test of all the samples cured at 2 days in orange, 7 days in green and 28 days in light-blue: (a) R42, (b) R39, (c) R36, (d) MK42, (e) MK39 and (f) MK36. (For interpretation of the references to colour in this figure legend, the reader is referred to the Web version of this article.)

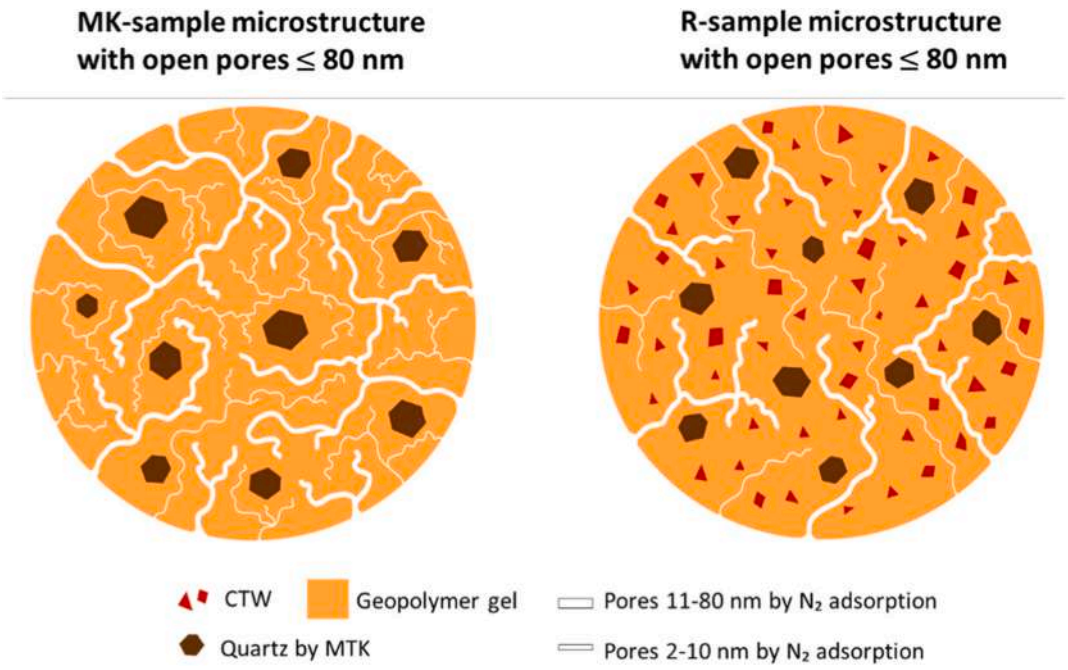

Fig. 8. Schematic representation of microstructures containing only the nano-porosity determined by N_2 adsorption analysis.

50 s and step size of 0.013°. Data were processed by the HighScore Plus software (PANalytical).

Scanning electron microscopy (SEM-EDS): Secondary electron images were acquired by using a Tescan Mira3 FEG-SEM (beam voltage = 15 kV and Working distance = 10 mm), coupled with an Energy Dispersive X-ray Spectroscopy (EDS, Bruker) probe. Samples were made conductive before SEM observations by gold sputtering with a Quorum Q 150 ES sputter coater.

Geometric density, water absorption and mechanical properties: to assess the properties of the final products, geometric density, water absorption and compressive strength measurements were carried out. At least three cylindrical samples with a diameter of 35 mm and a height of 20 mm for each formulation were used for measuring geometric density and water absorption values. Geometric density was measured by dividing dry mass (obtained by oven exposure at 100 °C for at least 24 h) by geometric volume. Water absorption test was carried out by immersing dry samples (after recording dry mass values, m_d) in demineralised water for at least 24 h to reach water saturation. Water absorption values (WA%) were assessed by weighing the samples in saturated surface-dry condition (m_{ssd}) according to Eq. (1):

$$WA\% = ((m_{ssd} - m_d) \ / \ m_d) \cdot 100 \quad (1)$$

Finally, the mechanical performance was assessed by measuring compressive strength on at least 5 samples obtained by halving prismatic samples of 40 mm × 40 mm × 160 mm. Compressive strength test was carried out by using an Amsler–Wolpert equipment and by applying a constant displacement rate of 5 mm/min, in accordance with EN 196-1 [71].

3. Results and discussion

3.1. Porosity and structural analysis

Open porosity assessment of MK- and R-samples was first carried out by MIP and the outcomes are reported in Figs. 4 and 5. The cumulative pore size distribution of all samples is reported in Fig. 4 by comparing geopolymers made of 100 % MTK with those obtained by combining MTK and CTW as precursors. The following observations can be drawn.

- the partial replacement of MTK with CTW induces the formation of a slightly more porous microstructure compared to that obtained by MTK alone at the same curing time;
- reducing the w/s ratio leads to a decrease in intruded Hg, thus promoting the development of denser microstructures in the investigated porosity range. Similar effects are also reported in the literature for different combinations of precursors (e.g. CTW/carbon fly ash [20], forest biomass ash/metakaolin [72], diatomite/GGBS [55]);
- "ink-bottle" porosity, intended as the portion of the Hg intruded volume that remains inside the sample after lowering the pressure at the end of MIP analysis, ranges between 33 and 53% (Fig. 4d). For both MK- and R-samples, it generally decreases with increasing the curing time. For R-samples, where both MTK and CTW were used as precursors, the "ink-bottle" amount is generally lower than that of the MK-samples and it shows an increasing trend when the w/s ratio decreases. The obtained "ink-bottle" porosity values are consistent with previous findings on fly ash-based geopolymers [7]; this large fraction, mainly associated with capillary pore formation during 3D network development [7], may result in an underestimation of pore size [19,66,].

Of great interest is also the evolution of open pore size as a function of the curing time, as highlighted in Fig. 5, where derivative pore size distributions are reported. R-samples, where both MTK and CTW are used as precursors, exhibit a broader pore size distribution compared to samples prepared with 100% MTK. For example, the pore size distributions of R42 and MK42 samples are in 0.01 – 1 μm and 0.01 – 0.4 μm ranges, respectively. Both distributions become slightly narrower by increasing the curing time and with the decrease in w/s, thanks to the refinement of large pores. The formulations prepared with a w/s ratio of 0.39 (plots *b* and *e* in Fig. 3) exhibit the best micropore evolution irrespective of the precursor system, whether MTK alone or the combined MTK–CTW precursors are employed. Indeed, the refinement is very effective for the MK39 samples, in which mainly monomodal pore-size distributions are present and progressively shift to lower pore sizes with increasing curing time. A similar shifting is observed for R39; however, pore distributions are multimodal with large pores still present at 28 days of curing. Such behaviour can be related to the lower

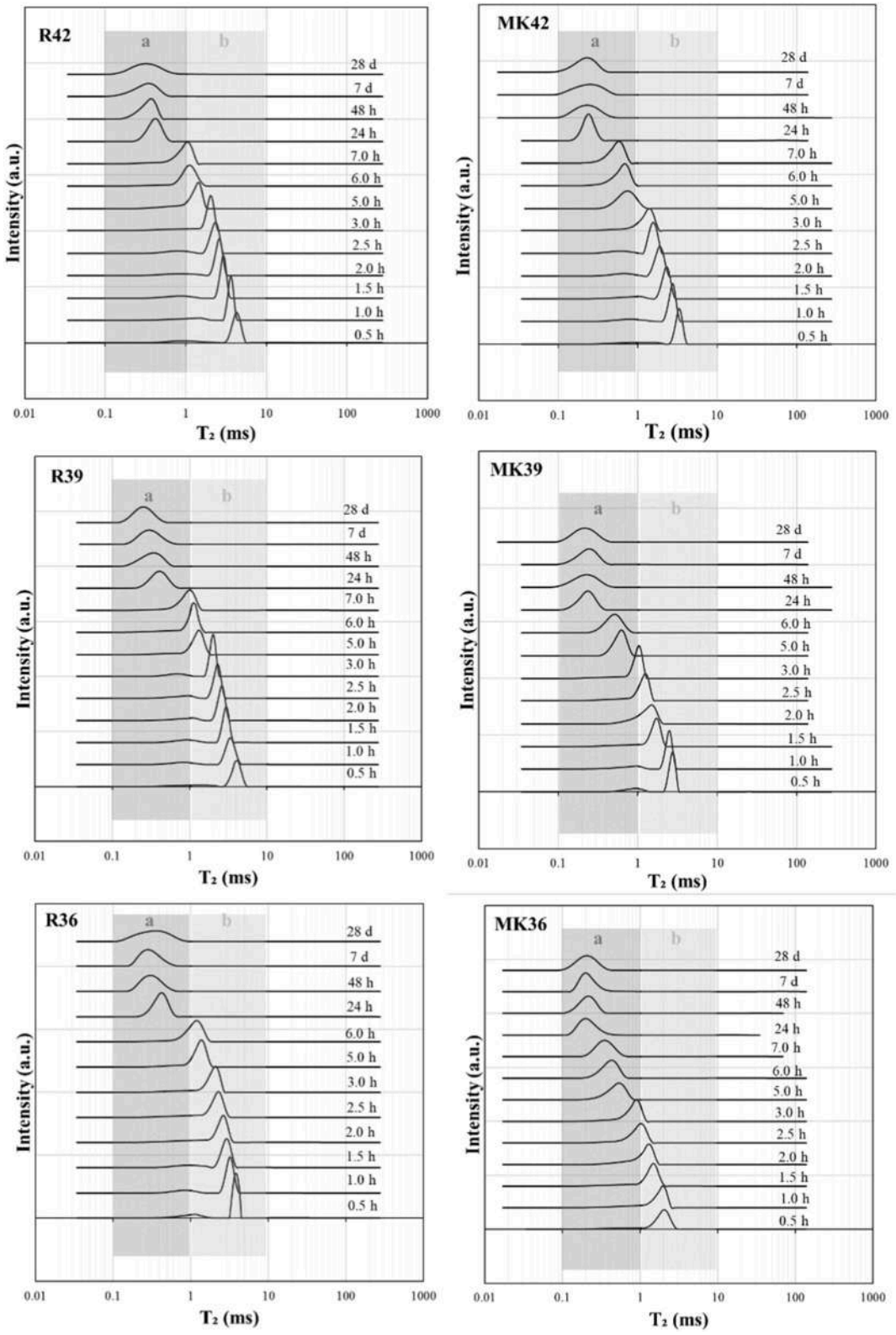

Fig. 9. T_2 distributions of the investigated samples at different curing times up to 28 days. Region "a" represents "water in gel pores" (0.1 - 1.0 ms) and region "b" represents "water in capillary pores" (1.0 – 10.0 ms).

reactivity of CTW. Indeed, even if CTW exhibits a higher amount of amorphous silica compared to MTK and consequently R-based geopolymers have a higher theoretical SiO_2/Al_2O_3 ratios than MK-based samples (Table 3), it shows significantly smaller specific surface area and specific pore volume compared to MTK, thus limiting its reactivity. The higher particle size distribution observed for MTK in Fig. 1b and Table 2 is apparent and it is due to the agglomeration of MTK particles, as observed in Fig. 2. Such agglomeration, which is a typical phenomenon of the flash calcination production process of the applied MTK [63, 64], does not interfere with MTK reactivity, which remains very high

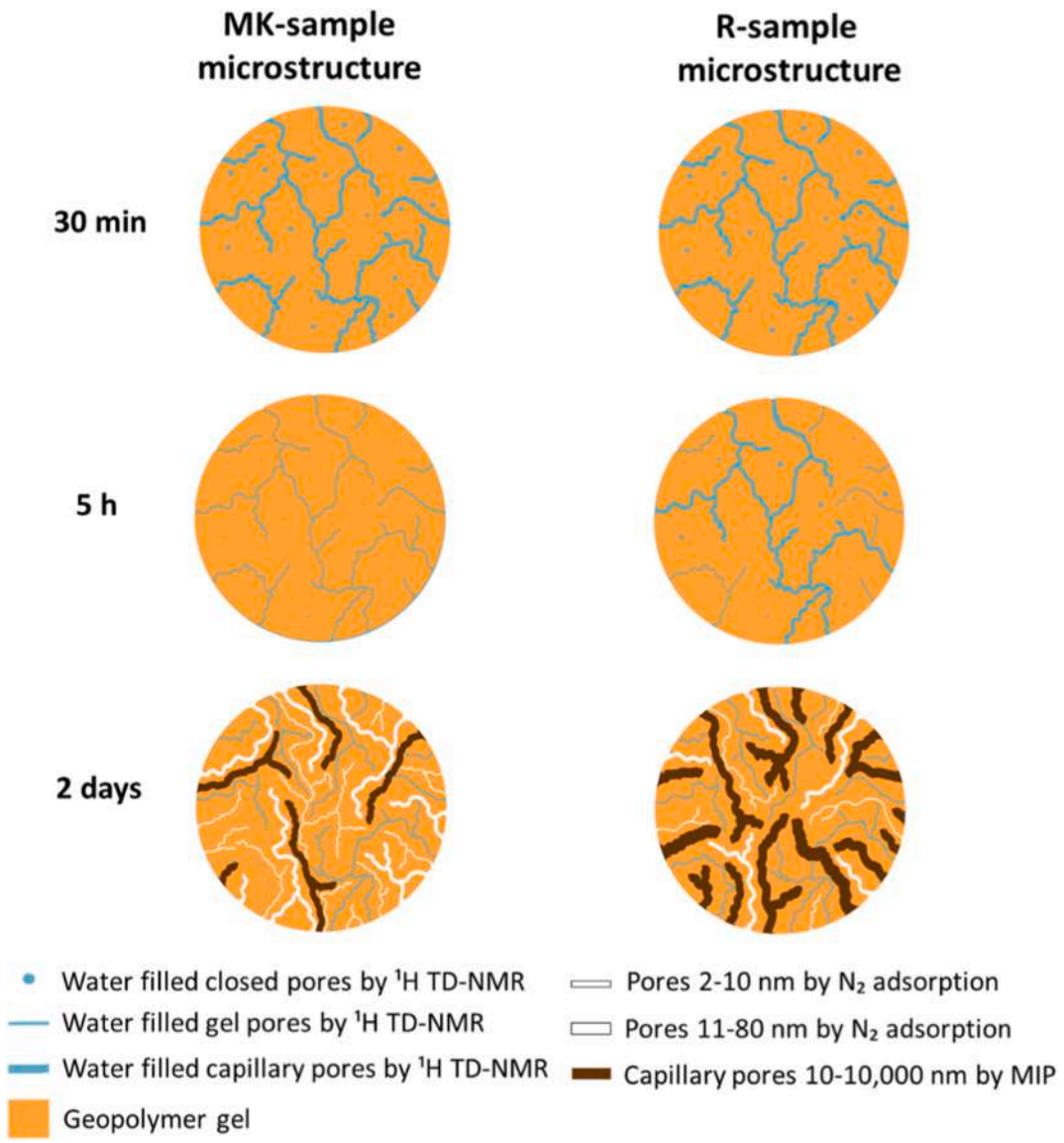

Fig. 10. Schematic representation of microstructures at different curing times determined by MIP, N_2 adsorption test and ^{1}H TD-NMR techniques. Only porosities are represented for clarity's sake.

thanks to its high pore volume that allows a very effective contact between MTK fine particles and alkaline solutions.

To investigate the mesoporous microstructures, N_2 adsorption/desorption isotherms were also recorded to analyse the pore size distribution in the range of 2 – 80 nm as a function of curing time. Type IV isotherms with a hysteresis loop were found for all the investigated samples (Fig. 6), as already observed for metakaolin [44] and metakaolin/slag [46] geopolymers. However, the characteristic shape of the isotherms and the volume of N_2 adsorbed per unit volume of specimen change significantly if one or two precursors are involved in the geopolymerization.

When MTK and CTW are combined in the mix design, the absorbed N_2 volume is lower than when only MTK is present. This behaviour, which occurs regardless of the w/s ratio and curing time, agrees with the findings of Duxson [44], who observed lower N_2 absorption for higher Si/Al ratios. Finally, the hysteresis loop becomes larger for MK geopolymers and occurs at lower relative pressures, indicating a more effective adsorption/desorption behaviour.

From adsorption-desorption isotherms, cumulative pore volumes are obtained as reported in Table 4: values are in the range of 0.015 – 0.029 cm^3/g and 0.025 – 0.055 cm^3/g for R- and MK-samples, respectively.

For all the series, the pore volumes increase with curing time due to a higher amount of gel formation. The lowest nano-pore volume detected for R-samples, regardless of the w/s ratio, can be due to the presence of a very compact gel and/or to a minor amount of gel formed according to a lower reactivity of CTW.

The derivative pore size distributions obtained by N_2 adsorption test (Fig. 7) show that nano-pore dimensions are very similar for all the samples cured at different curing times, thus indicating that the increase in the observed nano-pore volume can be ascribed only to a higher content of gel when MTK is used as precursor. Fig. 8 presents a schematic of the microstructure for MK- and R-samples, showing only the nano-porosity detected by N_2 adsorption analysis. For R-samples, the presence of a large amount of unreacted CTW particles is highlighted as the cause of the lower gel content compared to MK-geopolymers.

To investigate how a 3D network is formed since the very early stage, ^{1}H TD-NMR technique has been applied. The results of T_2 distributions are reported in Fig. 9. All the samples exhibit a unimodal T_2 distribution centred between 0.1 and 5 ms according to the curing time, as detected in other studies based both on metakaolin- and slag-based alkali activated materials [55,56,]. At a very early stage of curing, i.e. 0.5 – 1.5 h, a small peak was recorded at a shorter relaxation time equal to 1.0 ms.

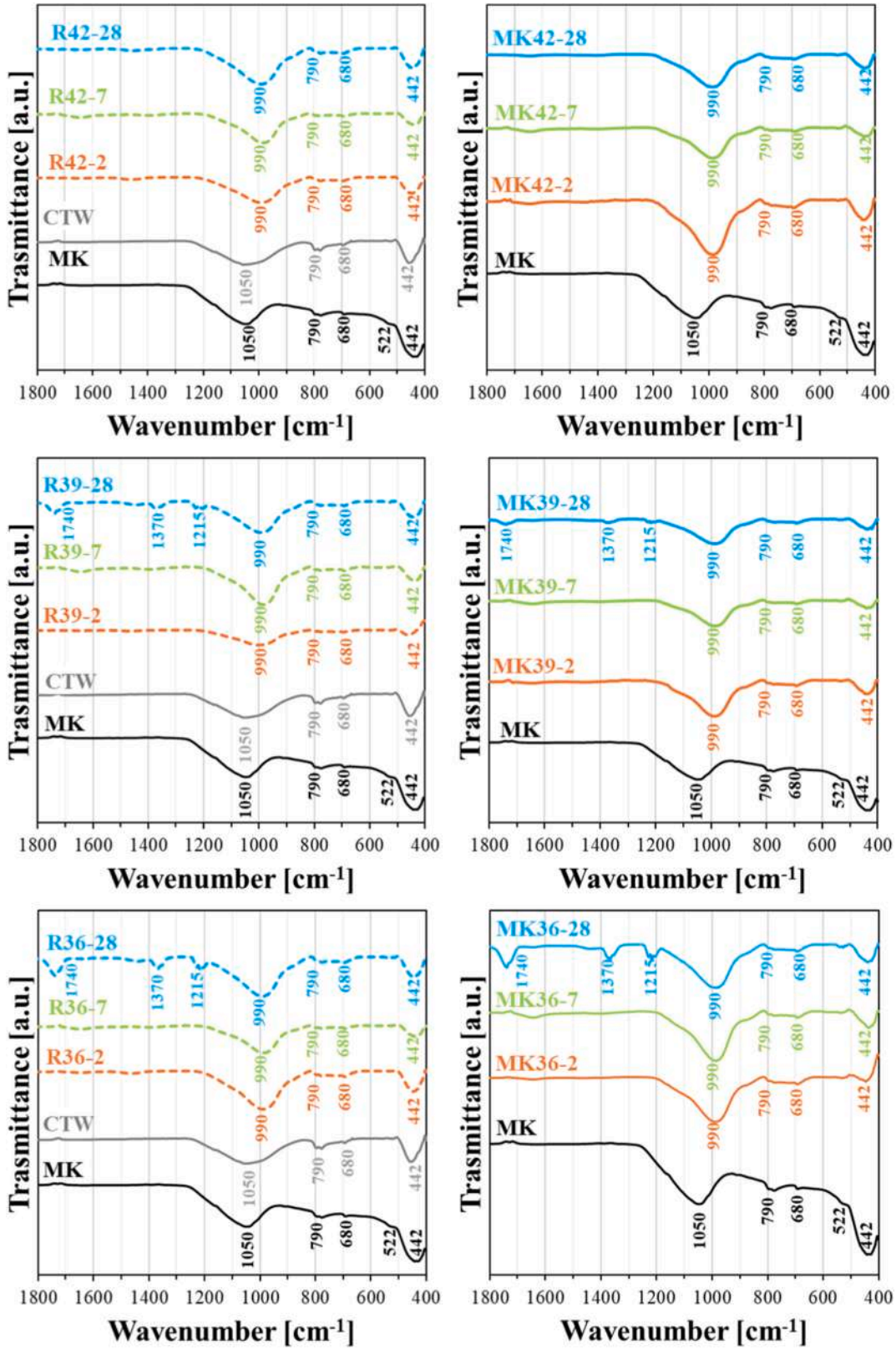

Fig. 11. FT-IR spectra of the geopolymers cured at 2 days in orange, 7 days in green and 28 days in light-blue. In each plot, FT-IR spectra of the precursors (MTK and CTW) are reported in black and grey, respectively. (For interpretation of the references to colour in this figure legend, the reader is referred to the Web version of this article.)

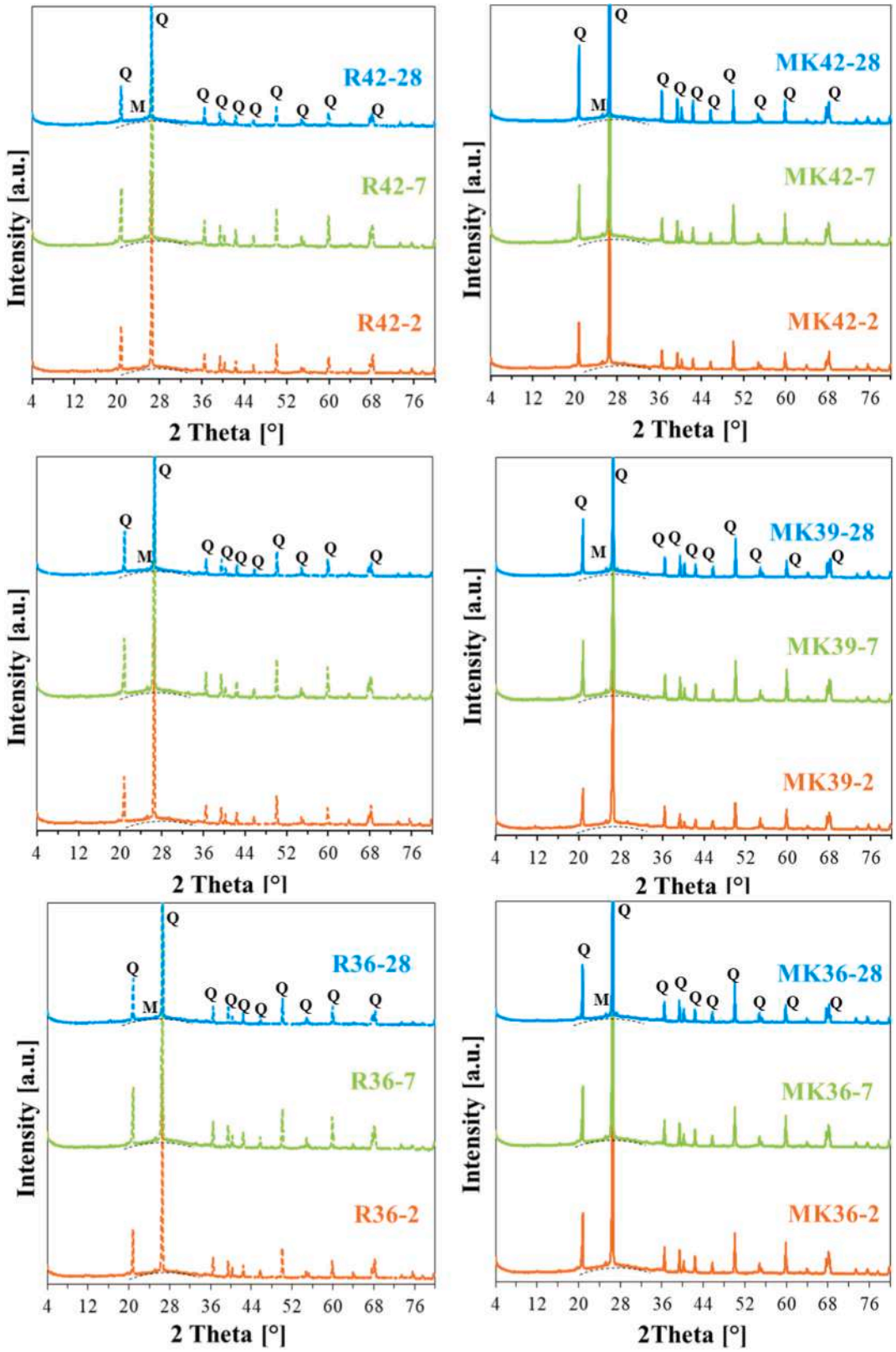

Fig. 12. XRD patterns of the geopolymers cured at 2 days in orange, 7 days in green and 28 days in light-blue. (For interpretation of the references to colour in this figure legend, the reader is referred to the Web version of this article.)

While curing progresses, the T_2 peaks shift towards shorter T_2 times, whereas the total signal intensity is almost constant (results not shown for brevity's sake). These two phenomena suggest that water becomes increasingly confined within the smaller pores formed during the development of the 3D network, and primarily serves as a reaction medium during the cross-linking process [73–75]. In previous studies [55,56], two different regions that represent the water in different pore types have been defined based on T_2 values: “water in gel pores” in the

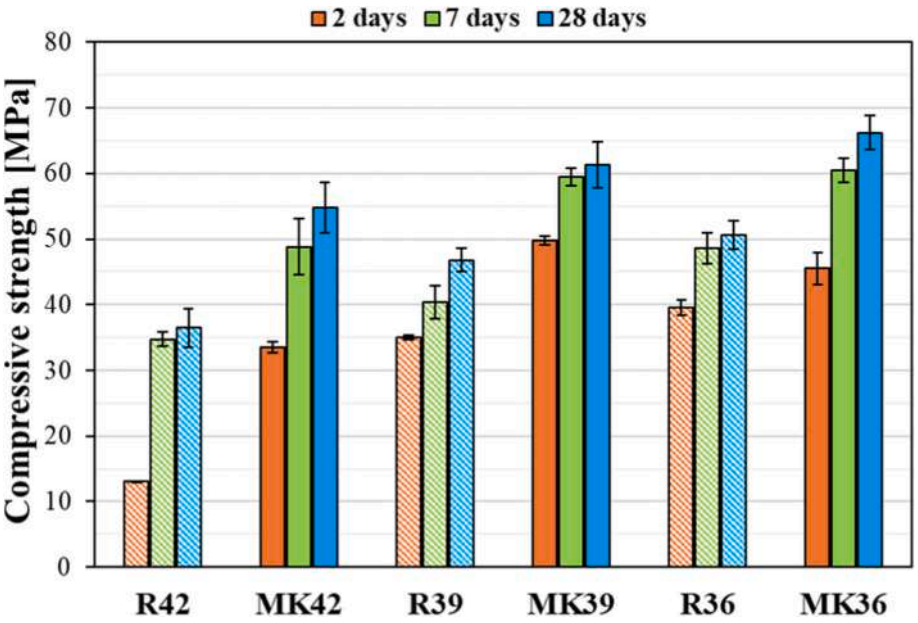

Fig. 13. Compressive strength of the geopolymers cured at 2 days in orange, 7 days in green and 28 days in light-blue. (For interpretation of the references to colour in this figure legend, the reader is referred to the Web version of this article.)

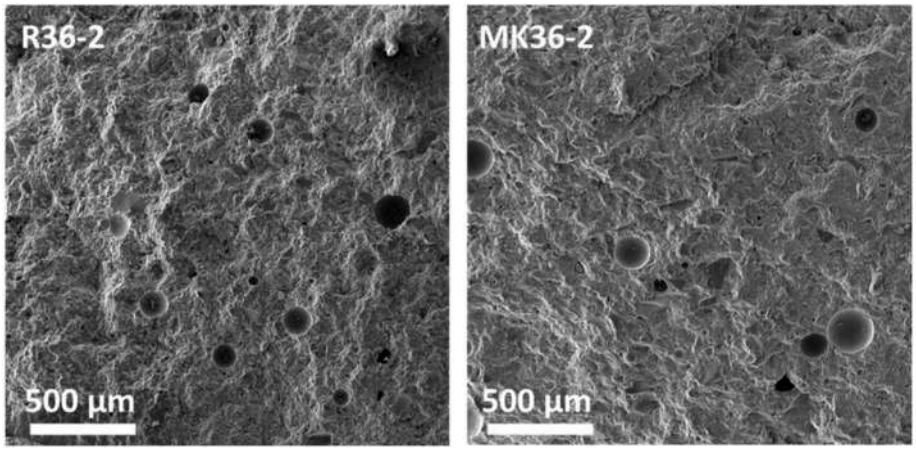

Fig. 14. Evidence of air voids in the microstructures of R36 and MK36 at 2 days of curing.

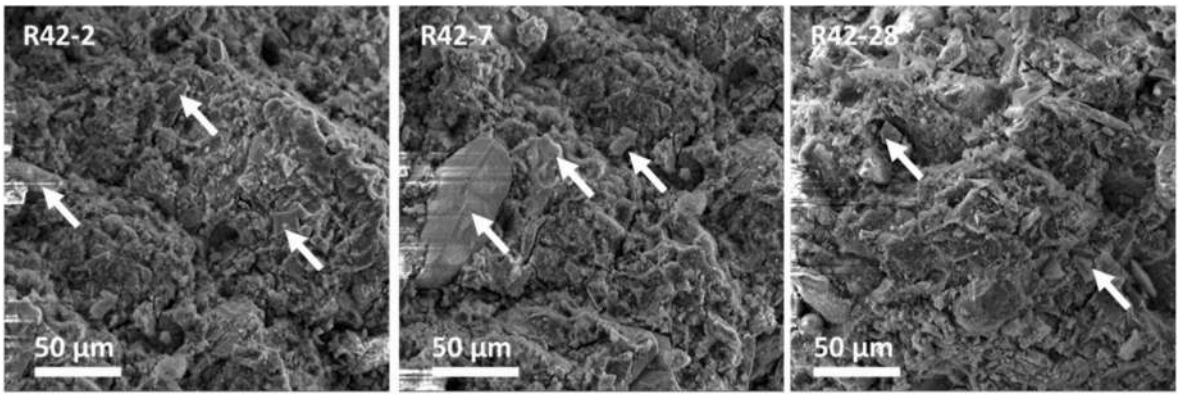

Fig. 15. SEM images of R42 at different curing times (2, 7 and 28 days). White arrows indicate the presence of unreacted CTW particles.

range of 0.1 – 1.0 ms (region "a" in Fig. 7) and "water in capillary pores" in the range of 1.0 – 10 ms (region "b" in Fig. 7). For all MK-samples, complete gel-pore formation was achieved after 5-6 h of curing. A slight effect of w/s ratio was observed for MK-42, which required slightly longer (6 h) to complete the process. The partial replacement of MTK with CTW induced a delay for the main T_2 peak to fully enter the

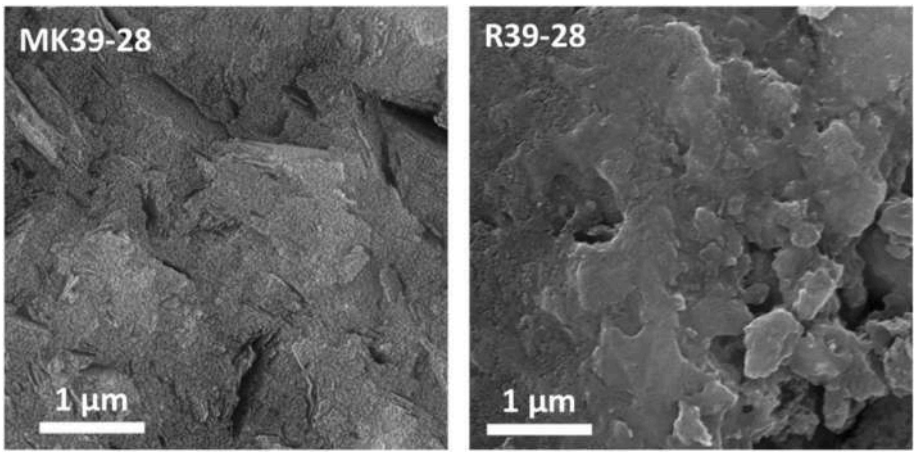

Fig. 16. Comparison of microstructures for MK39 and R39 at 28 days of curing.

region "a" and mitigate the effect of the different w/s. This indicates that the presence of CTW prolongs the total reaction process for 3D network formation, as also observed in the case of diatomite addition in alkali activated slag cements [55]. Anyway, after 24 h, the main T_2 peak fully enters the region "a" characteristic for the gel pores and remains stable at 0.2 – 0.3 ms for all the samples. It is also important to note that for curing times longer than 24 h, no differences are observed in the T_2 distribution, thus indicating that most of the water is in the gel pore space and the 3D network formation is basically complete. Eventual air-filled pores (their formation can occur due to air entrapment during casting of the samples) are not visible with this technique, as it measures the relaxation time of hydrogen nuclei. The obtained results clearly indicate that CTW contributes to the formation of the three-dimensional network, imparting a slight but discernible retardation in gel formation.

The application of MIP, BET and ^{1}H TD-NMR techniques provides complementary insights into the microstructural evolution at the different curing stages of the samples. However, it should be noted that each technique relies on distinct physical principles and underlying assumptions. More in detail, MIP works in the range of 0.01-100 µm, is sensitive to pore entry sizes and connectivity, and it also measures "ink-bottle" porosity. It is based on forced non-wetting liquid penetration (Hg) on the sample and data elaboration is based on the assumption that all open pores are cylindrical. N_2 adsorption provides access to open pores in the range of 2-80 nm and specific surface area under dried conditions. It assumes equilibrium adsorption and the adopted model introduces interpretation uncertainty. ^{1}H TD-NMR only captures the distribution of water-filled pores in a non-destructive manner, giving relaxation time as a result. Thus, it represents an indirect method for assessing pore size distribution, based on the inverse proportionality between relaxation time (T_2) and the surface-to-volume ratio. Short relaxation time indicates small porosities.

Considering the distinct assumptions underlying the three instrumental techniques, the experimental results for MK- and R-geopolymers have been schematically summarized to illustrate, as an example, the multiscale evolution of porosity within their microstructure at selected curing times (Fig. 10). At the very early stage of hydration (e.g. 30 min), water-filled capillary pores and water-filled closed pores are represented according to the experimental findings obtained by ^{1}H TD-NMR. The progressive refinement of water-filled capillary pores into water-filled gel pores was also monitored using the same technique. Based on the experimental data, this refinement is depicted as completed after 5 h for the MK-samples, whereas for R-samples it remains incomplete, with the coexistence of both capillary and gel pores schematically illustrated. For the hardened samples (i.e. after 2 days of curing), the schematic representation reveals open nano- and micro-porosity for both sample series, as determined by N_2 adsorption and MIP measurements.

Therefore, the application of this multi-analytical approach, integrating three complementary techniques, overcomes the limitations inherent to any single method and serves as an effective tool for advancing the understanding of microstructural evolution. To provide complementary information on 3D network formation, FT-IR data are reported in Fig. 11. FT-IR spectra were acquired at all curing times, and, for comparison, spectra of both precursors (MTK and CTW) are also reported. MTK and CTW spectra show similar features, due to their similar nature as aluminosilicates; thus this analytical technique does not provide significant insights into the effect of CTW addition in MK-samples. Contributions at 1050-1052 cm^{-1}, 780-794 cm^{-1}, 672-686 cm^{-1} and 434-442 cm^{-1} can be ascribed to Si–O–Si stretching vibration, Al–O stretching vibration, vibration of Al–O–Si and bending of Si–O–Si, respectively. MTK also shows a small shoulder around 522 cm^{-1} to be ascribed to the bending of Si–O–Al [19,36,43,46,76,77]. The main difference comparing the spectra of the precursors with the ones of the MK- and R-samples is the shifting of the band around 1050 cm^{-1} (Si–O–Si stretching) to 980-1000 cm^{-1} related to Si–O–Al stretching vibration. This difference confirms the occurrence of the geopolymerization due to the alkaline environment and consequent formation of 3D networks [43, 78]. Moreover, at 28 days of curing time, all samples, except R42 and MK42, show new and low-intensity bands at 1364-1387 cm^{-1} and 1215 cm^{-1}, 1737-1740 cm^{-1} that are related to the bending of OH of water molecule and formation of C–O bonds, respectively. This is in accordance with efflorescence formation ruled by carbonation reaction [79]. To confirm the effect of the applied precursors on the 3D network formation, XRD patterns of all the geopolymers at the three different curing times are reported in Fig. 12. Mainly quartz and in lower amount mullite are present as crystalline phases in all the geopolymers. These phases that are not involved in the alkali activation are sourced from the applied precursors, as shown in Fig. 2b. Differently from XRD patterns of MTK and CTW (Fig. 2b), which exhibit a halo peak in the range of $2\theta = 17 - 30°$, indicating the amorphous content of both the precursors typical for aluminosilicate glasses, in all the geopolymers, the broad halo peak shifts to higher 2θ values in the range of $2\theta = 20 - 35°$, thus demonstrating the typical behaviour of alkali activation of aluminosilicate precursors under XRD analysis [79,80,]. Lastly, no other newly formed crystalline phases, such as zeolites or sodium silicate and/or carbonate, have been detected in XRD patterns, confirming FT-IR results.

3.2. Physical, mechanical and microscopy characterizations

The physical and mechanical properties of the two series of geopolymers were investigated in terms of geometric density, water absorption and compressive strength after 2, 7 and 28 days of curing time.

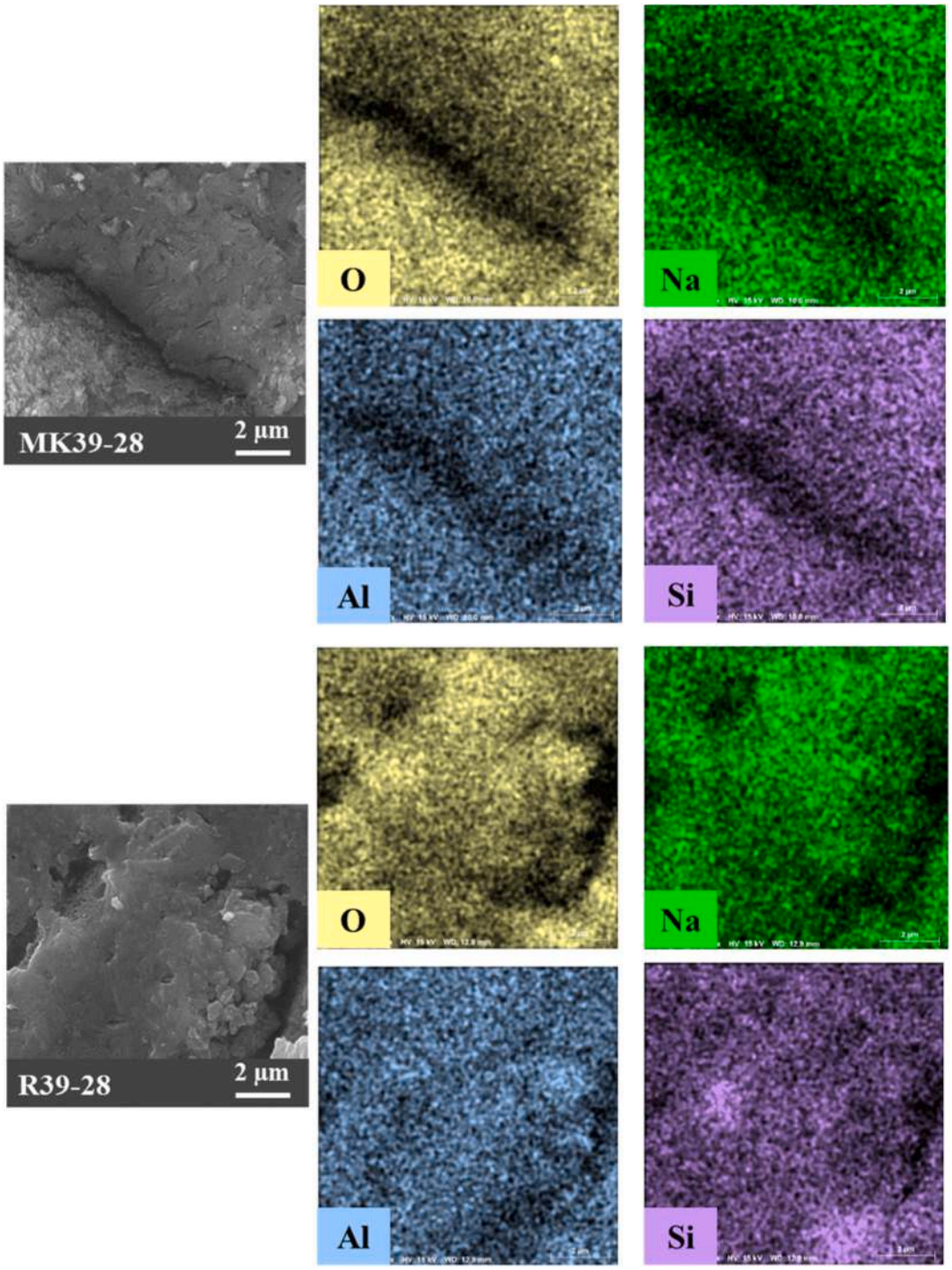

Fig. 17. X-ray maps of the microstructure of MK39 and R39 at 28 days of curing. The typical elements present in geopolymers, i.e. O, Na, Si and Al are reported.

All the samples show geometric density around 1.6 g/cm^3 and water absorption values around 20 – 21%, independent of the curing time and the formulation. Conversely, the compressive strength exhibits distinct trends as reported in Fig. 13. Notably, compressive strength increases with curing time, particularly from 2 to 7 days. From 7 to 28 days of curing, no significant strength improvement is observed (considering the error bars). This indicates that the development of mechanical properties is nearly complete at 7 days, regardless of the precursor used. Moreover, compressive strength is also influenced by the w/s ratio. For both MK- and R-samples, reducing w/s from 0.42 to 0.39 leads to an evident improvement in strength performances. These behaviours can be interpreted in relation to porosity results as follows: (i) the ^{1}H TD-NMR data at 7 and 28 days (Fig. 9) show that the peaks associated with the gel porosity nearly overlap, indicating a comparable gel-pore structure and, consequently, similar load-bearing capacity, which is consistent with comparable compressive strength values; (ii) the MIP results (Fig. 5) reveal a narrowing of the monomodal pore size distribution within the 0.01–1 µm range when the w/s ratio decreases from 0.42 to 0.39. This refinement of capillary porosity likely contributes to a denser microstructure, improving stress distribution and potentially enhancing mechanical performance. However, the additional reduction to w/s equal to 0.36 has not been particularly beneficial because the mix resulted in too viscous and some air bubbles remained entrapped during casting procedures. Indeed, a large number of air voids (some of which

with a diameter >50 μm) have been observed by SEM, as reported in Fig. 14. Air trapping is often observed in alkali activated systems because alkaline activators, especially sodium silicate solution, exhibit higher density and viscosity compared to water-based solutions [7–9].

The partial replacement of MTK with CTW leads to a significant reduction in compressive strength; however, R39 and R36 samples reached values greater than 35 MPa at 7 days of curing time. These results are notable and in accordance with those reported in the literature for porcelain stoneware powder-based alkali activated mortars [25]. Moreover, the effect of CTW in decreasing compressive strength is also coherent with the results obtained by MIP and N_2 adsorption previously discussed, where a coarsening of micropores in the range 0.01-1 μm and a lower content of geopolymer gel have been disclosed, respectively.

Further SEM observations are reported in Fig. 15, where some unreacted particles of CTW are observed in R42 at all curing times, confirming their lower reactivity compared to MTK.

By increasing the curing time, a densification of the microstructure is observed for both MK- and R-samples; however, some differences are noted from the morphological point of view (Fig. 16). When only MTK is used as a precursor, the densification leads to a very compact morphology where the plate-like particles of MTK appear condensed, forming a continuous gel phase. When MTK and CTW are combined, two distinct morphologies - one continuous and one granular –leading to a more porous microstructure are observed, thus confirming the results obtained by MIP. Finally, X-ray maps of O, Na, Si and Al for MK39-28 and R39-28 (obtained via EDS analysis) are shown in Fig. 17. It is clearly visible that these four elements are distributed homogeneously in the analysed portion of the samples, indicating the formation of a 3D network of sodium aluminosilicates [75].

4. Conclusions

In this study, the effects of combining ceramic tile waste (CTW) and metakaolin (MTK) as precursors for geopolymers were elucidated through a multi-analytical investigation of micro- and nano-porous features, complemented by physical and mechanical characterization.

The main findings can be summarized as follows.

- replacing metakaolin with 35% CTW leads to a coarsening of pore size distributions in the 0.08-1.00 μm range and a reduction in gel content. Although a delay in the development of the 3D network was observed, the gel formation process was nevertheless completed within 24 h. The resulting microstructure produced a lower compressive strength compared to MK-samples; however, strengths still exceeded 30 MPa after at least 7 days of curing. These results indicate that CTW is a viable and promising precursor for alkali activation;
- decreasing the w/s ratio from 0.42 to 0.36 causes several changes in the microstructure of the geopolymers, regardless of the precursors. The best performance was achieved with a w/s ratio of 0.39. At the highest w/s ratio (0.42), MIP detected an increase in open porosity within the 0.01–1 μm range, resulting in reduced mechanical properties. Conversely, at the lowest w/s ratio (0.36), the formation of closed pores due to trapped air limits potential gains in mechanical strength;
- the multi-analytical approach adopted in this study - monitoring pore evolution at different curing times using three complementary techniques (MIP, N_2 adsorption, and ^{1}H TD-NMR) – integrated the strengths of each method, providing a clear and comprehensive picture of microstructural changes. This type of integrated investigation has been applied for the first time to geopolymers derived from two precursors, thereby advancing the knowledge in geopolymer science.

Finally, although the variability of the investigated CTW is likely limited - since it originates from the rectification process of fired porcelain stoneware tiles, whose formulations are generally similar worldwide - additional research gaps remain to be addressed, particularly regarding the long-term durability of the investigated mixes and their industrial scalability.

CRediT authorship contribution statement

Giulia Masi: Writing – original draft, Visualization, Validation, Supervision, Methodology, Data curation, Conceptualization. **Carlotta Pacente:** Writing – original draft, Visualization, Investigation, Data curation. **Lucia Ferrari:** Writing – original draft, Validation, Supervision, Methodology, Investigation. **Anastasiia Nagmutdinova:** Investigation, Data curation. **Elisa Franzoni:** Writing – review & editing, Validation, Supervision. **Maria Chiara Bignozzi:** Writing – review & editing, Validation, Supervision, Resources, Project administration, Funding acquisition, Conceptualization.

Declaration of competing interest

The authors declare that they have no known competing financial interests or personal relationships that could have appeared to influence the work reported in this paper.

Acknowledgements

This study was performed within the scope of the “Product and process sustainability for the production of tiles” project in the framework of Programma Operativo Nazionale (PON) "Ricerca e Innovazione" 2014 – 2020 (ai sensi dell'art. 24, comma 3, lett. a), della Legge 30 dicembre 2010, n. 240 e s.m.i. e del D.M. 10 agosto 2021 n. 106) of the Italian Ministry of University and Research (green thematic area). Lucia Ferrari acknowledges the MICS (Made in Italy – Circular and Sustainable) Extended Partnership as received funding from the European Union Next-Generation EU (Piano Nazionale di Ripresa e Resilienza (PNRR) – Missione 4 Componente 2, Investimento 1.3 – D.D. 1551.11-10-2022, PE00000004).

References

[1] Y. Wu, B. Lu, T. Bai, H. Wang, F. Du, Y. Zhang, L. Cai, C. Jiang, W. Wang, Geopolymer, green alkali activated cementitious material: synthesis, applications and challenges, Constr. Build. Mater. 224 (2019) 930–949, https://doi.org/10.1016/j.conbuildmat.2019.07.112.

[2] J.L. Provis, Alkali-activated materials, Cem. Concr. Res. 114 (2018) 40–48, https://doi.org/10.1016/j.cemconres.2017.02.009.

[3] C. Shi, B. Qu, J.L. Provis, Recent progress in low-carbon binders, Cem. Concr. Res. 122 (2019) 227–250, https://doi.org/10.1016/j.cemconres.2019.05.009.

[4] G. Masi, S. Manzi, M.C. Bignozzi, Gender balance in construction material research: the analysis of alkali-activated materials by a bibliometric study using scopus database, Front. Mater. 7 (2020), https://doi.org/10.3389/fmats.2020.572514.

[5] S.A. Bernal, E.D. Rodríguez, A.P. Kirchheim, J.L. Provis, Management and valorisation of wastes through use in producing alkali-activated cement materials, J. Appl. Chem. Biotechnol. 91 (2016) 2365–2388, https://doi.org/10.1002/jctb.4927.

[6] F. Winnefeld, A. Leemann, M. Lucuk, P. Svoboda, Assessment of phase formation in alkali activated low and high calcium fly ashes in building materials, Constr. Build. Mater. 24 (6) (2010) 1086–1093, https://doi.org/10.1016/j.conbuildmat.2009.11.007.

[7] G. Masi, W.D.A. Rickard, L. Vickers, M.C. Bignozzi, A. van Riessen, A comparison between different foaming methods for the synthesis of light weight geopolymers, Ceram. Int. 40 (9A) (2014) 13891–13902, https://doi.org/10.1016/j.ceramint.2014.05.108.

[8] W.D.A. Rickard, R. Williams, J. Temuujin, A. van Riessen, Assessing the suitability of three Australian fly ashes as an aluminosilicate source for geopolymers in high temperature applications, Mater. Sci. Eng. A 528 (9) (2011) 3390–3397, https://doi.org/10.1016/j.msea.2011.01.005.

[9] M.C. Bignozzi, S. Manzi, M.E. Natali, W.D.A. Rickard, A. van Riessen, Room temperature alkali activation of fly ash: the effect of Na_2O/SiO_2 ratio, Constr. Build. Mater. 69 (2014) 262–270, https://doi.org/10.1016/j.conbuildmat.2014.07.062.

[10] F. Puertas, M. Palacios, H. Manzano, J.S. Dolado, A. Rico, J.A. Rodríguez, Model for the C-A-S-H gel formed in alkali-activated slag cements, J. Eur. Ceram. Soc. 31 (12) (2011) 2043–2056, https://doi.org/10.1016/j.jeurceramsoc.2011.04.036.

[11] M. Amran, G. Murali, N. Hafizah A. Khalid, R. Fediuk, T. Ozbakkaloglu, Y.H. Lee, S. Haruna, Y.Y. Lee, Slag uses in making an ecofriendly and sustainable concrete: a review, Constr. Build. Mater. 272 (2021) 121942, https://doi.org/10.1016/j.conbuildmat.2020.121942.
[12] S. Ghorbani, L. Stefanini, Y. Sun, B. Walkley, J.L. Provis, G. De Schutter, S. Matthys, Characterisation of alkali-activated stainless steel slag and blast-furnace slag cements, Cem. Concr. Comp. 143 (2023) 105230, https://doi.org/10.1016/j.cemconcomp.2023.105230.
[13] M. Criado, B. Walkley, X. Ke, J.L. Provis, S.A. Bernal, Slag and activator chemistry control the reaction kinetics of sodium metasilicate-activated slag cements, Sustainability 10 (12) (2018) 4709, https://doi.org/10.3390/su10124709.
[14] J. He, J. Zhang, Y. Yu, G. Zhang, The strength and microstructure of two geopolymers derived from metakaolin and red mud-fly ash admixture: a comparative study, Constr. Build. Mater. 30 (5) (2012) 80–91, https://doi.org/10.1016/j.conbuildmat.2011.12.011.
[15] A. Kumar, S. Kumar, Development of paving blocks from synergistic use of red mud and fly ash using geopolymerization, Constr. Build. Mater. 38 (2) (2013) 865–871, https://doi.org/10.1016/j.conbuildmat.2012.09.013.
[16] D.D. Dimas, I.P. Giannopoulou, D. Panias, Utilization of alumina red mud for synthesis of inorganic polymeric materials, Miner. Process. Extr. Metall. Rev. 30 (3) (2009) 211–239, https://doi.org/10.1080/08827500802498199.
[17] W. Hajjaji, A. Andrejkovičová, C. Zanelli, M. Alshaaer, M. Dondi, J.A. Labrincha, F. Rocha, Composition and technological properties of geopolymers based on metakaolin and red mud, Mater. Des. 52 (24) (2013) 648–654, https://doi.org/10.1016/j.matdes.2013.05.058.
[18] W.M. Kriven, C. Leonelli, J.L. Provis, A.R. Boccaccini, C. Attwell, V.S. Ducman, C. Ferone, S. Rossignol, T. Luukkonen, J.S.J. van Deventer, J.V. Emiliano, J. E. Lombardi, Why geopolymers and alkali-activated materials are key components of a sustainable world: a perspective contribution, J. Am. Ceram. Soc. 107 (2024) 5159–5177, https://doi.org/10.1111/jace.19828.
[19] Y. Ma, G. Wang, G. Ye, J. Hu, A comparative study on the pore structure of alkali-activated fly ash evaluated by mercury intrusion porosimetry, N_2 adsorption and image analysis, J. Mater. Sci. 53 (2018) 5958–5972, https://doi.org/10.1007/s10853-017-1965-x.
[20] T. Yang, H. Zhu, Z. Zhang, Influence of fly ash on the pore structure and shrinkage characteristics of metakaolin-based geopolymer pastes and mortars, Constr. Build. Mater. 153 (2017) 284–293, https://doi.org/10.1016/j.conbuildmat.2017.05.067.
[21] T. Yang, H. Zhu, Z. Zhang, X. Gao, C. Zhang, O. Wu, Effect of fly ash microsphere on the rheology and microstructure of alkali-activated fly ash/slag pastes, Cem. Concr. Res. 109 (2018) 198–207, https://doi.org/10.1016/j.cemconres.2018.04.008.
[22] I. Luhar, S. Luhar, M.M.A.B. Abdullah, M. Nabiałek, A.V. Sandu, J. Szmidla, A. Jurczynska, R.A. Razak, I.H.A. Aziz, N.H. Jamil, L.M. Deramanet, Assessment of the suitability of ceramic waste in geopolymer composites: an appraisal, Materials 14 (2021) 3279, https://doi.org/10.3390/ma14123279.
[23] G. Masi, A. Tugnoli, M.C. Bignozzi, Lightweight alkali activated composites by direct foaming based on ceramic tile waste and fly ash, Ceram. Int. 50 (24C) (2024) 55410–55420, https://doi.org/10.1016/j.ceramint.2024.10.399.
[24] Z.B. Öztürk, A. Eser, S. Çelikten, I.I. Atabey, High-temperature performance of geopolymer mortars containing ceramic filter press cake and pottery waste powders, Adv. Powder Tech. 36 (1) (2025) 104732, https://doi.org/10.1016/j.apt.2024.104732.
[25] A. Rezzoug, K. Ayed, N. Leklou, Thermal, mechanical and microstructural properties of geopolymer mortars derived from ceramic sanitary-ware wastes: pathway to net zero emission, Ceram. Int. 50 (24C) (2024) 55535–55545, https://doi.org/10.1016/j.ceramint.2024.10.414.
[26] L. Carabba, S. Manzi, E. Rambaldi, G. Ridolfi, M.C. Bignozzi, High-temperature behaviour of alkali-activated composites based on fly ash and recycled refractory particles, J. Ceram. Sci. Tech. 8 (3) (2017) 377–387, https://doi.org/10.4416/JCST2017-00047.
[27] E. Sassoni, P. Pahlavan, E. Franzoni, M.C. Bignozzi, Valorization of brick waste by alkali-activation: a study on the possible use for masonry repointing, Ceram. Int. 42 (13) (2016) 14685–14694, https://doi.org/10.1016/j.ceramint.2016.06.093.
[28] L. Reig, M.M. Tashima, L. Soriano, M. V Borrachero, J. Monzó, J. Payá, Alkaline activation of ceramic waste materials, WBV 4 (2013) 729–736, https://doi.org/10.1007/s12649-013-9197-z.
[29] H. Dahlbo, J. Bachér, K. Lähtinen, T. Jouttijärvi, P. Suoheimo, T. Mattila, S. Sironen, T. Myllymaa, K. Saramäki, Construction and demolition waste management - a holistic evaluation of environmental performance, J. Clean. Prod. 107 (2015) 333–341, https://doi.org/10.1016/j.jclepro.2015.02.073.
[30] G. Boschi, G. Bonvicini, G. Masi, M.C. Bignozzi, Recycling insight into the ceramic tile manufacturing industry, Open Ceram 16 (2023) 100471, https://doi.org/10.1016/j.oceram.2023.100471.
[31] Y. Deng, Z. Zhang, J. Hu, Q. Yu, C. Shi, Fundamental study on reactive components and leaching kinetics of ceramic waste for geopolymer production, Comp. B Eng. 295 (2025), https://doi.org/10.1016/j.compositesb.2025.112211.
[32] B. Horvat, V. Ducman, Potential of green ceramics waste for alkali activated foams, Materials 12 (2019), https://doi.org/10.3390/ma12213563.
[33] M.P. Bilondi, V. Ghaffarian, M. Amiri Daluee, R. Pakizehrooh, S.H. Tazik, A. Behzadian, M. Zaresefat, Experimental studies on mix design and properties of ceramic-glass geopolymer mortars using response surface methodology, Sci. Rep. 15 (2025) 282, https://doi.org/10.1038/s41598-024-82658-3.
[34] S.A. Bernal, J. Bejarano, C. Garzón, R.M. de Gutiérrez, S. Delvasto, E.D. Rodríguez, Performance of refractory aluminosilicate particle/fiber-reinforced geopolymer composites, Comp. B Eng. 43 (4) (2012) 1919–1928, https://doi.org/10.1016/j.compositesb.2012.02.027.
[35] Z. Bayer Ozturk, R. Cırık, İ.İ. Atabey, Sustainable environment approach by the usage of ceramic pottery waste in geopolymer mortar, IJEST 20 (2023) 7577–7588, https://doi.org/10.1007/s13762-023-04939-0.
[36] E.D. Yanti, L. Mubarok, Subari, B.D. Erlangga, E. Widyaningsih, Jakah, I. Pratiwi, A. Rinovian, T. Nugroho, B. Herbudiman, Utilization of various ceramic waste as fine aggregate replacement into fly ash-based geopolymer, Mater. Lett. 357 (2024) 135651, https://doi.org/10.1016/j.matlet.2023.135651.
[37] T.I. Ahmed, I.M. El-Mehasseb, N.M. El-Shafai, R.S. Salama, D.E. Tobbala, Investigation the mechanical, durability, heating struggle, thermal gravimetric examination, and microstructure of geopolymer ceramic concrete incorporating nano-silica and nano-soda-cans, Constr. Build. Mater. 467 (2025) 140325, https://doi.org/10.1016/j.conbuildmat.2025.140325.
[38] V. Kumar, P. Kumar, Self-compacted geopolymer concrete incorporating waste ceramic powder, multiscale and multidisciplinary modeling, Exp. Des. 7 (2024) 5187–5202, https://doi.org/10.1007/s41939-024-00510-7.
[39] M. Fugazzotto, G. Cultrone, P. Mazzoleni, G. Barone, Suitability of ceramic industrial waste recycling by alkaline activation for use as construction and restoration materials, Ceram. Int. 49 (6) (2023), https://doi.org/10.1016/j.ceramint.2022.11.111.
[40] A.M. Abdelmonem, A. Azam, A. Alruwaili, A.S. Ouda, M.A. Elrahman, Effect of ceramic tile waste addition on the performance of slag-based geopolymer upon exposure to marine conditions: physico-mechanical characteristics, and shielding proficiency against ionizing radiation, Sustain. Chem. Pharm. 43 (2025) 101886, https://doi.org/10.1016/j.scp.2024.101886.
[41] E. Kamseu, M. Cannio, E.A. Obonyo, F. Tobias, M.C. Bignozzi, V.M. Sglavo, C. Leonelli, Metakaolin-based inorganic polymer composite: effects of fine aggregate composition and structure on porosity evolution, microstructure and mechanical properties, Cem. Concr. Comp. 53 (2014) 258–269, https://doi.org/10.1016/j.cemconcomp.2014.07.008.
[42] M.C. Bignozzi, S. Manzi, I. Lancellotti, E. Kamseu, L. Barbieri, C. Leonelli, Mix-design and characterization of alkali activated materials based on metakaolin and ladle slag, Appl. Clay Sci. 73 (2013) 78–85, https://doi.org/10.1016/j.clay.2012.09.015.
[43] P. Rovnaník, Effect of curing temperature on the development of hard structure of metakaolin-based geopolymer, Constr. Build. Mater. 24 (7) (2010) 1176–1183, https://doi.org/10.1016/j.conbuildmat.2009.12.023.
[44] P. Duxson, J.L. Provis, G.C. Lukey, S.W. Mallicoat, W.M. Kriven, J.S.J. van Deventer, Understanding the relationship between geopolymer composition, microstructure and mechanical properties, Colloids Surf. A Physicochem. Eng. Asp. 269 (1–3) (2005) 47–58, https://doi.org/10.1016/j.colsurfa.2005.06.060.
[45] H. Chen, Y.J. Zhang, P.Y. He, Y. Zhang, Effective and eco-friendly seed-assisted synthesis of nanostructurally monolithic mordenite, Ferroelectrics 547 (1) (2019) 44–50, https://doi.org/10.1080/00150193.2019.1592482.
[46] X. Feng, S. Yan, S. Jiang, K. Huang, X. Ren, X. Du, P. Xing, Green synthesis of the metakaolin/slag based geopolymer for the effective removal of methylene blue and Pb (II), Silicon 14 (2022) 6965–6979, https://doi.org/10.1007/s12633-021-01439-z.
[47] P. Arokiasamy, M.M.A.B. Abdullah, S.Z.A. Rahim, A.V. Sandu, A. Fedrigo, R. Ediati, S. Ishak, N.H.M. Kaus, Hydroxyapatite incorporated metakaolin/sludge based geopolymer adsorbent for copper ions and ciprofloxacin removal: synthesis, characterization and mechanisms, Arab. J. Chem. 17 (5) (2024) 105745, https://doi.org/10.1016/j.arabjc.2024.105745.
[48] M.B. Jaji, G.P.A.G. van Zijl, A.J. Babafemi, Slag-modified metakaolin-based 3D printed geopolymer: mechanical characterisation, microstructural properties, and nitrogen physisorption pore analysis, J. Build. Eng. 81 (2024) 108166, https://doi.org/10.1016/j.jobe.2023.108166.
[49] K.S.W. Sing, D.H. Everett, R.A.W. Haul, L. Moscou, R.A. Pierotti, J. Rouquerol, T. Siemieniewska, Reporting physisorption data for gas/solid systems with special reference to the determination of surface area and porosity, Pure Appl. Chem. 57 (1985) 603–619, https://doi.org/10.1351/pac198557040603.
[50] M. Thommes, K. Kaneko, A.V. Neimark, J.P. Olivier, F. Rodriguez-Reinoso, J. Rouquerol, K.S.W. Sing, Physisorption of gases, with special reference to the evaluation of surface area and pore size distribution (IUPAC technical report), Pure Appl. Chem. 87 (9-10) (2015) 1051–1069, https://doi.org/10.1515/pac-2014-1117.
[51] A.M. Gajewicz, E. Gartner, K. Kang, P.J. McDonald, V. Yermakou, A ^{1}H NMR relaxometry investigation of gel-pore drying shrinkage in cement pastes, Cem. Concr. Res. 86 (2016) 12–19, https://doi.org/10.1016/j.cemconres.2016.04.013.
[52] A.C.A. Muller, K.L. Scrivener, A.M. Gajewicz, P.J. McDonald, Densification of C-S-H measured by ^{1}H NMR relaxometry, J. Phys. Chem. C 117 (1) (2013) 403–412, https://doi.org/10.1021/jp3102964.
[53] L. Ferrari, A. Nagmutdinova, A. Müller, N. Mikanovic, M. Ben-Haha, V. Bortolotti, E. Franzoni, Disclosing the mechanism behind rheological challenges in calcined clay-based cements, Constr. Build. Mate.r 492 (2025) 142837, https://doi.org/10.1016/j.conbuildmat.2025.142837.
[54] A. Nagmutdinova, L. Brizi, C. Testa, V. Bortolotti, L. Ferrari, A comparative study of OPC, WPC, and LC3 cements by low-field 1H TD NMR, Constr. Build. Mater. 506 (2026) 144785, https://doi.org/10.1016/j.conbuildmat.2025.144785.
[55] G. Liang, W. Yao, Effect of diatomite on the reaction kinetics, early-age chemical shrinkage and microstructure of alkali-activated slag cements, Constr. Build. Mater. 376 (2023) 131026, https://doi.org/10.1016/j.conbuildmat.2023.131026.
[56] G. Liang, W. Yao, A. She, New insights into the early-age reaction kinetics of metakaolin geopolymer by ^{1}H low-field NMR and isothermal calorimetry, Cem. Concr. Comp. 137 (2023) 104932, https://doi.org/10.1016/j.cemconcomp.2023.104932.

[57] J. Li, S. Mailhiot, A.M. Kantola, H. Niu, H. Sreenivasan, V.V. Telkki, P. Kinnunen, Longitudinal single-sided NMR study: Silica-to-alumina ratio changes the reaction mechanism of geopolymer, Cem. Concr. Res. 160 (2022) 106921, https://doi.org/10.1016/j.cemconres.2022.106921.
[58] C. Bai, K. Zheng, F. Sun, X. Wang, L. Zhang, T. Zheng, P. Colombo, B. Wang, A review on metakaolin-based porous geopolymers, Appl. Clay Sci. 258 (2024) 107490, https://doi.org/10.1016/j.clay.2024.107490.
[59] Z. Yu, R. de Oliveira-Silva, Y. Pontikes, D. Sakellariou, Low-field 1H NMR study on geopolymers: the effect of paramagnetic Fe(III), Cem. Concr. Res. 166 (2023) 107116, https://doi.org/10.1016/j.cemconres.2023.107116.
[60] B. Swathi, R. Vidjeapriya, Influence of precursor materials and molar ratios on normal, high, and ultra-high performance geopolymer concrete – a state of art review, Constr. Build. Mater. 392 (2023) 132006, https://doi.org/10.1016/j.conbuildmat.2023.132006.
[61] R. San Nicolas, M. Cyr, G. Escadeillas, Characteristics and applications of flash metakaolins, Appl. Clay Sci. 83–84 (2013) 253–262, https://doi.org/10.1016/j.clay.2013.08.036.
[62] R. Pouhet, M. Cyr, R. Bucher, Influence of the initial water content in flash calcined metakaolin-based geopolymer, Constr. Build. Mater. 201 (2019) 421–429, https://doi.org/10.1016/j.conbuildmat.2018.12.201.
[63] R. San Nicolas, M. Cyr, G. Escadeillas, Performance-based approach to durability of concrete containing flash-calcined metakaolin as cement replacement, Constr. Build. Mater. 55 (2014) 313–322, https://doi.org/10.1016/j.conbuildmat.2014.01.063.
[64] G. Masi, A. Saccani, M.C. Bignozzi, Influence of different waste-derived fillers in extruded geopolymeric matrix for 3D printing, Mater. Today Proc. (2023), https://doi.org/10.1016/j.matpr.2023.06.184.
[65] S. Brunauer, P.H. Emmett, E. Teller, Adsorption of gases in multimolecular layers, J. Am. Chem. Soc. 60 (2) (1938) 309–319, https://doi.org/10.1021/ja01269a023.
[66] R.A. Cook, K.C. Hover, Mercury porosimetry of hardened cement pastes, Cem. Concr. Res. 29 (1999) 933–943, https://doi.org/10.1016/S0008-8846(99)00083-6.
[67] C. Gallé, Effect of drying on cement-based materials pore structure as identified by mercury intrusion porosimetry: a comparative study between oven-, vacuum-, and freeze-drying, Cem. Concr. Res. 31 (2001) 1467–1477, https://doi.org/10.1016/S0008-8846(01)00594-4.
[68] Z. Yu, G. Ye, The pore structure of cement paste blended with fly ash, Constr. Build. Mater. 45 (2013) 30–35, https://doi.org/10.1016/j.conbuildmat.2013.04.012.
[69] S. Diamond, A critical comparison of mercury porosimetry and capillary condensation pore size distributions of Portland cement pastes, Cem. Concr. Res. (1971) 531–545, https://doi.org/10.1016/0008-8846(71)90058-5.
[70] J. Landers, G.Y. Gor, A.V. Neimark, Density functional theory methods for characterization of porous materials, Colloids Surf. A Physicochem. Eng. Asp. 437 (2013) 3–32, https://doi.org/10.1016/j.colsurfa.2013.01.007.
[71] V. Bortolotti, R.J.S. Brown, P. Fantazzini, G. Landi, F. Zama, Uniform penalty inversion of two-dimensional NMR relaxation data, Inverse Probl. 33 (1) (2016) 015003, https://doi.org/10.48550/arXiv.1609.00324.
[72] EN 196-1:2016 Methods of Testing Cement - Part 1, Determination of strength, 2016.
[73] S. Candamano, P. De Luca, P. Frontera, F. Crea, Production of geopolymeric mortars containing forest biomass ash as partial replacement of metakaolin, Environ. Times 4 (2017) 74, https://doi.org/10.3390/environments4040074.
[74] J. Li, S. Mailhiot, H. Sreenivasan, A.M. Kantola, M. Illikainen, E. Adesanya, L. Kriskova, V.V. Telkki, P. Kinnunen, Curing process and pore structure of metakaolin-based geopolymers: liquid-state ^{1}H NMR investigation, Cem. Concr. Res. 143 (2021) 106394, https://doi.org/10.1016/j.cemconres.2021.106394.
[75] S. Park, M. Pour-Ghaz, What is the role of water in the geopolymerization of metakaolin? Constr. Build. Mater. 182 (2018) 360–370, https://doi.org/10.1016/j.conbuildmat.2018.06.073.
[76] P. Duxson, S.W. Mallicoat, G.C. Lukey, W.M. Kriven, J.S.J. van Deventer, The effect of alkali and Si/Al ratio on the development of mechanical properties of metakaolin-based geopolymers, Colloids Surf. A Physicochem. Eng. Asp. 292 (1) (2007) 8–20, https://doi.org/10.1016/j.colsurfa.2006.05.044.
[77] I. Lancellotti, M. Catauro, C. Ponzoni, F. Bollino, C. Leonelli, Inorganic polymers from alkali activation of metakaolin: effect of setting and curing on structure, J. Solid State Chem. 200 (2013) 341–348, https://doi.org/10.1016/j.jssc.2013.02.003.
[78] V.F.F. Barbosa, K.J.D. MacKenzie, C. Thaumaturgo, Synthesis and characterisation of materials based on inorganic polymers of alumina and silica: sodium polysialate polymers, Int. J. Inorg. Mater. 2 (4) (2000) 309–317, https://doi.org/10.1016/S1466-6049(00)00041-6.
[79] W.M. Kriven, J.L. Bell, M. Gordon, Microstructure and microchemistry of fully-reacted geopolymers and geopolymer matrix composites, Ceram. Trans. 153 (2004) 227–250.
[80] Z. Zhang, J.L. Provis, X. Ma, A. Reid, H. Wang, Efflorescence and subflorescence induced microstructural and mechanical evolution in fly ash-based geopolymers, Cem. Concr. Comp. 92 (2018) 165–177, https://doi.org/10.1016/j.cemconcomp.2018.06.010.